AFRL-PR-WP-TR-2003-2069

TIME AND SPACE RESOLVED HEAT TRANSFER – BOILING AND DROPLET COOLING STUDIES USING MICROHEATERS
Droplet and Spray Cooling Heat Transfer

Jungho Kim

University of Maryland
Department of Mechanical Engineering
College Park, MD 20742

APRIL 2003

Final Report for 01 June 1998 – 01 April 2003

PROPULSION DIRECTORATE
AIR FORCE RESEARCH LABORATORY
AIR FORCE MATERIEL COMMAND
WRIGHT-PATTERSON AIR FORCE BASE, OH 45433-7251

NOTICE

USING GOVERNMENT DRAWINGS, SPECIFICATIONS, OR OTHER DATA INCLUDED IN THIS DOCUMENT FOR ANY PURPOSE OTHER THAN GOVERNMENT PROCUREMENT DOES NOT IN ANY WAY OBLIGATE THE US GOVERNMENT. THE FACT THAT THE GOVERNMENT FORMULATED OR SUPPLIED THE DRAWINGS, SPECIFICATIONS, OR OTHER DATA DOES NOT LICENSE THE HOLDER OR ANY OTHER PERSON OR CORPORATION; OR CONVEY ANY RIGHTS OR PERMISSION TO MANUFACTURE, USE, OR SELL ANY PATENTED INVENTION THAT MAY RELATE TO THEM.

THIS REPORT IS RELEASABLE TO THE NATIONAL TECHNICAL INFORMATION SERVICE (NTIS). AT NTIS, IT WILL BE AVAILABLE TO THE GENERAL PUBLIC, INCLUDING FOREIGN NATIONS.

THIS TECHNICAL REPORT HAS BEEN REVIEWED AND IS APPROVED FOR PUBLICATION.

RENGASAMY PONNAPPAN
Senior Mechanical Engineer
Energy Storage & Thermal Sciences Branch

JOHN K. ERBACHER
Acting Branch Chief
Energy Storage & Thermal Sciences Branch

C. SCOTT RUBERTUS
Acting Deputy Chief
Power Division

Do not return copies of this report unless contractual obligations or notice on a specific document requires its return.

REPORT DOCUMENTATION PAGE

The public reporting burden for this collection of information is estimated to average 1 hour per response, including the time for reviewing instructions, searching existing data sources, searching existing data sources, gathering and maintaining the data needed, and completing and reviewing the collection of information. Send comments regarding this burden estimate or any other aspect of this collection of information, including suggestions for reducing this burden, to Department of Defense, Washington Headquarters Services, Directorate for Information Operations and Reports (0704-0188), 1215 Jefferson Davis Highway, Suite 1204, Arlington, VA 22202-4302. Respondents should be aware that notwithstanding any other provision of law, no person shall be subject to any penalty for failing to comply with a collection of information if it does not display a currently valid OMB control number. **PLEASE DO NOT RETURN YOUR FORM TO THE ABOVE ADDRESS**.

1. REPORT DATE *(DD-MM-YY)*	2. REPORT TYPE	3. DATES COVERED *(From - To)*
April 2003	Final	06/01/1998 – 04/01/2003

4. TITLE AND SUBTITLE

TIME AND SPACE RESOLVED HEAT TRANSFER – BOILING AND DROPLET COOLING STUDIES USING MICROHEATERS

Droplet and Spray Cooling Heat Transfer

5a. CONTRACT NUMBER
N/A

5b. GRANT NUMBER
F33615-98-1-2791

5c. PROGRAM ELEMENT NUMBER
62203F

6. AUTHOR(S)

Jungho Kim

5d. PROJECT NUMBER
3145

5e. TASK NUMBER
20

5f. WORK UNIT NUMBER
C6

7. PERFORMING ORGANIZATION NAME(S) AND ADDRESS(ES)

University of Maryland
Department of Mechanical Engineering
College Park, MD 20742

8. PERFORMING ORGANIZATION REPORT NUMBER

9. SPONSORING/MONITORING AGENCY NAME(S) AND ADDRESS(ES)

Propulsion Directorate
Air Force Research Laboratory
Air Force Materiel Command
Wright-Patterson Air Force Base, OH 45433-7251

10. SPONSORING/MONITORING AGENCY ACRONYM(S)
AFRL/PRPS

11. SPONSORING/MONITORING AGENCY REPORT NUMBER(S)
AFRL-PR-WP-TR-2003-2069

12. DISTRIBUTION/AVAILABILITY STATEMENT
Approved for public release; distribution is unlimited.

13. SUPPLEMENTARY NOTES
This report contains color.

Grant administered through University of Denver, Denver, CO.

14. ABSTRACT *(Maximum 200 Words)*
Heat transfer by phase change has long been an attractive method of cooling since large amounts of heat can be removed with relatively small temperature differences. The current study focused on making detailed measurements of the heat flux and interfacial motion of isolated droplets (with and without gas) as they impacted an isothermal surface at low and moderate superheats. The heat flux measurements were made using a novel heater array which allowed the local, instantaneous heat flux to be resolved. The results without gas indicate that the vaporization process can be divided into two parts; a first part that is characterized by transient effective heat transfer coefficient, and a second part in which the heat transfer coefficient is constant. The results with gas indicate that a gas bubble can nucleate, grow, and merge within the liquid, resulting in an increase in the droplet diameter. The measurements indicate that significantly smaller droplet evaporation times can be achieved as a result of the increase in liquid-vapor surface area during bubble formation. Recent work on the effects of dissolved gas and subcooling on spray cooling is also discussed.

15. SUBJECT TERMS

spray cooling, droplet cooling, microheater array, dissolved gas, subcooling

16. SECURITY CLASSIFICATION OF:			17. LIMITATION OF ABSTRACT:	18. NUMBER OF PAGES	19a. NAME OF RESPONSIBLE PERSON (Monitor)
a. REPORT Unclassified	**b. ABSTRACT** Unclassified	**c. THIS PAGE** Unclassified	SAR	62	Rengasamy Ponnappan
					19b. TELEPHONE NUMBER *(Include Area Code)* (937) 255-2922

i

TABLE OF CONTENTS

LIST OF FIGURES

LIST OF TABLES

NOMENCLATURE

A	area of microscale heater array [m^2]
A_{av}	time averaged area of splat [m^2]
A_b	area of bubble [m^2]
A_i	area of individual heater [m^2]
A_D	area of splat [m^2]
c_p	specific heat [J/kg·K]
D	splat diameter [m]
$D_{b,i}$	bubble apparent inner diameter [m]
D_o	initial splat diameter [m]
d_{eq}	equivalent droplet diameter [m]
d_o	initial droplet diameter [m]
h	heat transfer coefficient [W/m^2·°C]
h_{av}	average heat transfer coefficient [W/m^2·°C]
h_{cal}	calculated heat transfer coefficient [W/m^2·°C]
H_d	height of spherical segment [m]
h_v	heat transfer coefficient due to vapor [W/m^2·°C]
h_{fg}	heat of vaporization [J/kg]
k	thermal conductivity [W/m·°C]
LSCA	liquid solid contact area [m^2]
LVCA	liquid vapor contact area [m^2]
N	number of heaters in array
m_d	mass of droplet [kg]
Q_e	energy required to evaporate a droplet [J]
Q_{meas}	measured total energy required to evaporate a droplet [J]
q	heat rate [W]
q''	heat flux [W/cm^2]
q_i''	heat flux from singe heater [W/m^2]
q''_{liq}	heat flux into the liquid [W/cm^2]

q''_{nc}	natural convection heat flux [W/cm^2]
q''_{raw}	total heat flux [W/cm^2]
q''_{sc}	substrate conduction heat flux [W/cm^2]
R_d	radius of spherical segment [m]
R_l	thermal resistance of liquid [^{o}C/W]
R_{th}	thermal resistance [^{o}C/W]
R_v	thermal resistance of vapor [^{o}C/W]
t	time [s]
T_a	ambient temperature [^{o}C]
t_e	total evaporation time [s]
T_o	initial droplet temperature [°C]
T_{sat}	saturation temperature [°C]
T_w	local wall temperature [°C]
t_{e1}	first stage evaporation time [s]
t_{e2}	second stage evaporation time [s]
t_e	total evaporation time ($= t_{e1} + t_{e2}$)[s]
t^*	dimensionless evaporation time ($= t/t_e$)
V	volume of droplet [m^3]
V_o	initial volume of droplet [m^3]
V_i	voltage across the individual ith heater element
v	impact velocity of droplet (m/s)

Greek Symbols

α	thermal diffusivity ($= k/\rho\, c_p$)
β	wetting parameter ($= D/d_o$)
δ	average film thickness [m]
Δt	time increment [s]
δ_{min}	minimum film thickness to support nucleation [m]
ε	effectiveness of evaporation
m	kinematic viscosity [kg/m·s]

θ liquid-solid contact angle [degree]

θ_o initial contact angle

θ_r receding contact angle

ρ_d liquid density [kg/m^3]

ρ_v vapor density [kg/m^3]

σ surface tension [kg/s^2]

FOREWORD

This final technical report is part of the contract deliverables under the contract F33615-98-1-2791. This contract was sponsored and administered by the Propulsion Directorate of the Air Force Research Laboratory (AFRL), Wright Patterson Air Force Base. The work was also supported by the Laboratory for Physical Sciences (LPS). The support of the Technical Monitor Dr. Rengasamy Ponnappan, Energy Storage and Thermal Sciences Branch, AFRL/PRPS, and Paul Boudreaux of LPS is gratefully acknowledged.

I. INTRODUCTION

The use of liquid droplets to cool heated surfaces is an important process in several industrial applications due to the large amounts of energy that can be extracted from the wetted surface at relatively low temperatures through the latent heat of evaporation. For example, spray cooling might be used to remove large amounts of energy from electronic devices while keeping temperature gradients small and junction temperatures below 85 °C. Through tailoring the spray pattern, spray cooling can be used to obtain high heat transfer rates coupled with good temperature uniformity across the sprayed surface, which is important in microelectronics where even small temperature gradients across the chip can cause component failure. Unfortunately, the work to date has largely been empirical, and a lack of predictive capability regarding spray cooling exists due to the complex nature of the heat removal process. With this motivation, the goal of the current work is to examine the fundamental behavior of the transient heat transfer characteristics of a dynamically impacting droplet, which represents a first step towards understanding the more complex problem of a complete spray.

When a droplet strikes a heated surface, it flattens into a thin disk or splat whose thickness is much smaller than the diameter of the droplet, and high heat fluxes can be obtained due to the formation and evaporation of a thin liquid film on the heated surface. The controlling physical mechanism of the vaporization process depends on the degree of superheat applied to the heated surface. There are three distinct superheat regimes in connection with droplet vaporization from hot surfaces (Sadhal et al., 1997) – these are commonly referred to as the low, intermediate, and high superheat regime. In the low superheat case, the liquid droplet maintains contact with the surface, and nucleate boiling is typically suppressed for sufficiently thin drops. At intermediate superheat, nucleation takes place and heat transfer is enhanced. With increasing surface temperature, however, the droplet does not maintain continuous contact with the surface and the heat transfer rate decreases. In the high superheat regime, a stable vapor layer is formed between the droplet and the heated surface. In this regime, the droplet does not contact the solid wall and the heat transfer is limited mainly by conduction through a vapor layer. This mechanism is commonly referred to as the Leidenfrost phenomena.

Numerous investigations of the theoretical and experimental evolution of single droplet cooling heat transfer have been presented in literature reviews by Bolle and Moureau (1982) and Sadhal et al. (1997). Wachters and Westerling (1966a) and Wachters et al. (1966b) examined the kinematic motion of a single droplet impacting a hot surface using high-speed photographs above the Leidenfrost temperature. McGinnis and Holman (1969) investigated the effect of droplet velocity and impact frequency on the heat transfer rate, but also at temperatures above Leidenfrost. Toda (1972, 1974) reported extensive measurements of an evaporating water droplet and proposed a heat transfer model based on three regions (low temperature, transitional, and high temperature), according to the thermal behavior of the thin liquid film formed on the heated surface. Bonacina et al. (1979) performed experiments at low enough water flow rates to avoid the formation of a thin liquid film on the heated surface, resulting in a droplet evaporative cooling process. Liu and Yao (1982) introduced a model of spray cooling heat transfer based on the different heat transfer mechanisms involved in each region, and interpreted the contribution of each mechanism to the overall heat transfer. This model was again used by Choi and Yao (1987) in a study of spray cooling in the nucleate and film boiling regimes. diMarzo and Evans (1989) performed a significant amount of work for droplet evaporation on surfaces below the saturation temperature.

One method of enhancing the heat transfer beyond these levels is to add dissolved gas to the liquid so that the splat increases in size as bubbles within the droplet grow, resulting in an increase in the solid/liquid and liquid vapor contact area. The bubble may also cause an increase in heat transfer within the drop, if the liquid film around the bubbles thins locally. Qiao and Chandra (1997) have demonstrated that addition of a surfactant to droplets or sprays can increase the boiling heat transfer by up to 300%. For temperatures below boiling, the principal effect of the surfactant was to reduce the liquid-solid contact angle, increasing the surface area wetted by liquid. Above the boiling temperature, nucleation occurred at many more sites within the drop and foaming was observed. Cui et al. (2000) studied the effect of dissolved gases or solids on droplet heat transfer. Carbon dioxide gas or a salt was dissolved in water and videos of the evaporation process were obtained as the droplets struck a heated surface. For temperatures below and above the boiling point, the dissolved gas ($0.74 \ mm^3/mm^3$) was observed to increase the heat transfer slightly due to an increase in the splat circumference. When 1% by weight of $NaHCO_3$ was added to the liquid, it decayed when heated into Na_2CO_3 and CO_2. Foaming

within the droplet was observed to occur along with a large increase in heat transfer. Precipitation of Na_2CO_3 salt within the drop served as nucleation sites for boiling, and the CO_2 produced caused the droplet to swell, increasing the contact area. Milke et al. (1997) studied the effects of dissolved gas on spray evaporation using water. A Macor substrate was heated using three radiant panels. They found that cooling with gassy liquid resulted in a lower steady-state average temperatures, but attributed this to the decrease of radiant energy input to the surface when gassy liquid was used.

The objective of the current work is to study the fundamental mechanisms by which single droplets with and without dissolved gases transfer energy from heated surfaces. Time and space resolved heat transfer characteristics for a single droplet impacting a heated surface were experimentally measured using a novel experimental technique in which 96 individually controlled heaters were used to map the heat transfer coefficient contour on the surface. Visual observations of droplet behavior were also made using two high-speed digital video cameras and correlated to the heat transfer data. The present study was motivated by the need for an effective method of removing the high heat fluxes generated in compact electronic devices. Most such devices must operate at temperatures lower than 85 ^{o}C, so the saturation temperature of the coolant should be well below this temperature. PF-5060 is such a dielectric coolant, having a saturation temperature of 56 ^{o}C at atmospheric pressure. The properties of PF-5060 are identical to those of FC-72 (3M Corporation, 1995). The properties of PF-5060 are compared with those of water at Table 1.1.

1.1 Single Droplet Cooling Model Description

A two stage model of droplet evaporation was proposed by di Marzo and Evans (1989), di Marzo et al. (1993), and Qiao and Chandra (1997). A schematic of single droplet behavior and a typical side view of the droplet are shown in Figure 1. In the first stage, the contact splat diameter D remains constant while the contact angle θ decreases from its initial value θo to a receding value θr. In the second stage, the contact angle θ remains constant at θr while the splat diameter decreases.

Table 1.1. Physical properties of PF-5060 at 25$^{\text{o}}$C and 1 atm.

FLUIDS PROPERT	PF-5060	Water
Chemical Formula	C_6F_{14}	H_2O
BOILING POINT [$^{\text{O}}$C]	56	100
Density (ρ) [kg/m^3]	1,680	997
Dynamic Viscosity (*m*) [kg/m·s]	0.672×10^{-3}	0.901×10^{-3}
Kinematic Viscosity (ν) [m^2/s]	0.4×10^{-6}	0.904×10^{-6}
SURFACE TENSION (σ) [KG/S^2]	0.012	0.072
Specific Heat (c_p) [J/kg·K]	1046.5	4180
Thermal Conductivity (*k*) [W/m·K]	0.057	0.611
Latent Heat (h_{fg}) [kJ/kg]	87.9	2442.3
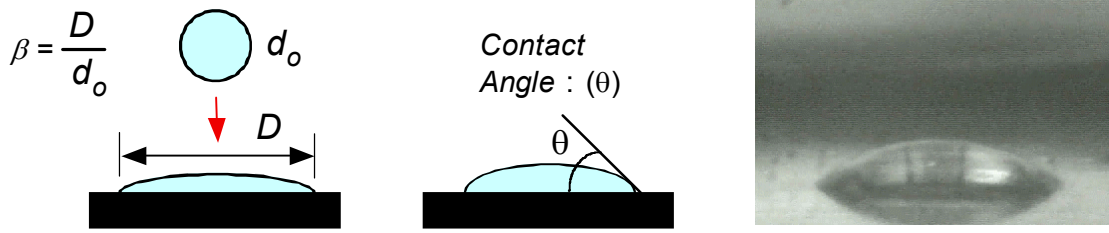
Figure 1.1. Schematic of single droplet and typical side view of droplet at 65 $^{\circ}$C.

The heat transfer coefficient for this droplet is defined as

$$h = \frac{q''_{liq}}{T_w - T_a}$$ (1)

An energy balance on the droplet is given by

$$hA(T_w - T_a) = -\rho_d h_{fg} \frac{dV}{dt}$$ (2)

where V is the volume of the droplet. V can be approximated by assuming the droplet is a segment of a sphere (Sadhal and Plesset ,1979) :

$$V = \frac{\pi D^3}{24} \frac{(1 - \cos\theta)^2 (2 + \cos\theta)}{\sin^3 \theta}$$ (3)

If h is assumed to be constant, then integrating Eq. (2) yields the value of h to be

$$h = \frac{V_0 \rho_d h_{fg}}{A_{av}(T_w - T_a)t_e}$$ (4)

where A_{av} is the time averaged contact area

$$A_{av} = \frac{1}{t_e} \int_0^{t_e} \frac{\pi}{4} d_o^2 \beta^2(t) \, dt$$ (5)

and t_e is the evaporation time for the droplet.

1.2 First Stage of Evaporation

During the first stage when the droplet diameter is the initial splat diameter D_o, the time rate of change of the droplet volume is given by

$$\frac{dV}{dt} = \frac{\pi D_0^3}{8} \left[\frac{1}{(1+\cos\theta)^2} \right] \frac{d\theta}{dt} \qquad (6)$$

Substituting Eq. (6) into Eq. (2) and integrating between θ_o and θ_r assuming h to be constant yields the time required for the first stage:

$$t_{e1} = \frac{\rho_d h_{fg} D_o}{4\, h\, (T_w - T_a)} \left[\tan\left(\frac{\theta_o}{2}\right) - \tan\left(\frac{\theta_r}{2}\right) + \frac{1}{3}\left(\tan^3\left(\frac{\theta_o}{2}\right) - \tan^3\left(\frac{\theta_r}{2}\right) \right) \right] \qquad (7)$$

1.2 Second Stage of Evaporation

During the second stage when the contact angle is equal to the receding contact angle ($\theta = \theta_r$) the time rate of change of the droplet volume is expressed by

$$\frac{dV}{dt} = \frac{\pi D^3}{8} \left[\frac{(1-\cos\theta_r)^2 (2+\cos\theta_r)}{\sin^3\theta_r} \right] \frac{dD}{dt} \qquad (8)$$

Substituting Eq. (8) into Eq. (2) and again assuming h is constant yields the rate at which the splat diameter changes with time:

$$\frac{dD}{dt} = -\frac{2h(T_w - T_a)}{\rho_d h_{fg} \left[\dfrac{(1-\cos\theta_r)^2 (2+\cos\theta_r)}{\sin^3\theta_r} \right]} \qquad (9)$$

Note that the splat diameter varies linearly for the given assumptions. Integrating yields the evaporation time t_{e2} required for the second stage:

$$t_{e2} = \frac{\rho_d h_{fg} D_0}{2h(T_w - T_a)} \left[\frac{(1-\cos\theta_r)^2 (2+\cos\theta_r)}{\sin^3\theta_r} \right] \qquad (10)$$

This model is used to determine the relative magnitude of the heat transfer resistance within the liquid to that of the vapor during droplet evaporation. Validation of the model described above is performed, and conclusions regarding the evaporation mechanism are made.

2. EXPERIMENTAL APPARATUS

An array of 96 individually controlled heaters was used to measure the heat flux distribution on the surface as a function of time and space. Feedback loops similar to those used in constant temperature anemometry are used to vary the voltage across each heater in the array to keep its temperature (resistance) constant, essentially eliminating the possibility of heater burnout. The electronics and heater array allowed for heat fluxes of up to 160 W/cm^2. The focus of the current experiments was to study the transient heat transfer distribution on the surface for given droplet impact parameters at three different superheats (85°C, 75°C, and 65°C).

2.1 Microscale Heater Array

Local surface heat flux and temperature measurements were provided by a serpentine platinum resistance heater element, similar to what was used in previous publications (Rule, et al.,1998, Rule and Kim, 1999, and Rule, et al.,1999). Each heater was 270 μm × 270 μm in size. The platinum heater lines were 5 μm wide, about 400 nm thick, spaced 5 μm apart, and about 600 μm in total length. Each heater had an electrical resistance of about 750 Ω. The 96 individual heaters were arranged in a square array about 2.7 mm on a side. A photograph of the microscale heater array is shown in Figure 2.1. The aluminum lines that supply power to the heaters were routed between the heaters to the edge of the array. Up to 17 heater arrays were fabricated simultaneously on a single quartz wafer using VLSI circuit fabrication techniques. Platinum was sputtered onto the entire wafer, the heaters were masked off, and the platinum was removed from the unmasked areas using an ion milling process. Aluminum was then vapor-deposited onto the surface, the aluminum power leads were masked off, and the remaining aluminum was removed using a wet chemical etch. As a final step, a layer of SiO$_2$ was deposited over the heater array to provide the surface with a uniform surface energy. The completed quartz wafer was diced into chips, each containing a single heater array. The chips were mounted on a pin-grid-array (PGA) package using epoxy adhesive, and the pins of the PGA were connected to the power leads of the heater array chip using a conventional wire-bonding technique. The completed package was then mounted in a PGA socket that was connected to the control and data-acquisition apparatus.
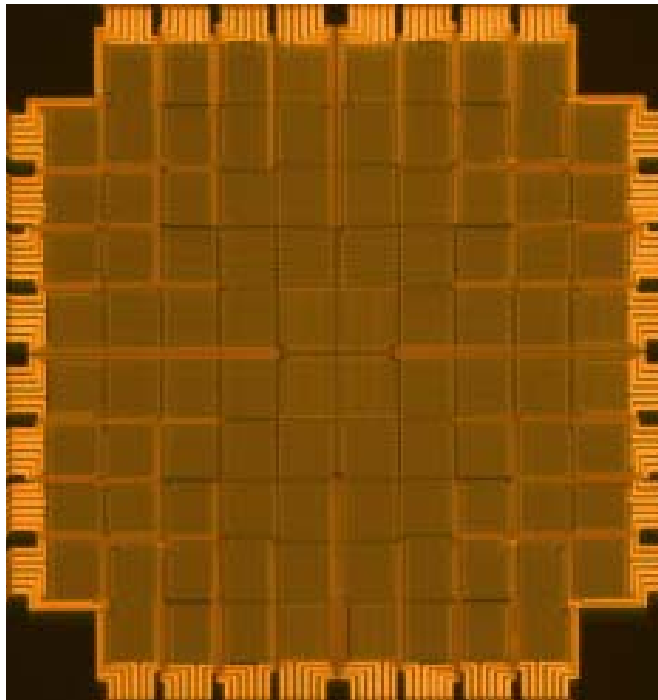
(a) Photo of 96 microscale heater arrays

	96	**95**	**94**	**93**	**92**	**91**	**90**	**89**	
65	**37**	**64**	**63**	**62**	**61**	**60**	**59**	**58**	**88**
66	**38**	**17**	**36**	**35**	**34**	**33**	**32**	**57**	**87**
67	**39**	**18**	**5**	**16**	**15**	**14**	**31**	**56**	**86**
68	**40**	**19**	**6**	**1**	**4**	**13**	**30**	**55**	**85**
69	**41**	**20**	**7**	**2**	**3**	**12**	**29**	**54**	**84**
70	**42**	**21**	**8**	**9**	**10**	**11**	**28**	**53**	**83**
71	**43**	**22**	**23**	**24**	**25**	**26**	**27**	**52**	**82**
72	**44**	**45**	**46**	**47**	**48**	**49**	**50**	**51**	**81**
	73	**74**	**75**	**76**	**77**	**78**	**79**	**80**	

(b) Heater numbering in array

Figure 2.1. Arrangement of 96 microscale heater arrays, with non-functional heaters represented by black squares.

2.2 Feedback Control Circuit

The temperature of heat heater in the array was kept at *constant temperature* by feedback circuits similar to those used in constant temperature anemometry (Figure 2.2). The electronics used in this series of tests were similar to those used in previous tests, and are described in detail in Bae, et al. (1999). The op-amp measured the imbalance in the bridge and output whatever voltage was needed to bring the bridge into balance. The heater resistance, and thus the heater temperature, was controlled by varying the resistance of a digital potentiometer from Dallas Semiconductor (DS1267). This chip consists of two 10 kΩ digital potentiometers, each having 256 wiper positions. The two potentiometers in this chip were connected in series to make a single 20 kΩ potentiometer with 512 wiper positions. Control of the wiper position was performed through a 3-wire serial interface to a personal computer and digital I/O card. For the resistor values indicated, a heater of nominally 750 Ω resistance could be varied over a 260 Ω range. The heaters have a temperature coefficient of resistance of nominally 0.002 °C^{-1}, providing a temperature range of approximately 175 °C. Since the digital potentiometer had 512 settings, the temperature of the heaters could be changed in 0.34 °C increments. The large 200 KΩ resistor at the top of the bridge was used to provide a small trickle current through the heater, and resulted in a voltage across the heater of about 100 mV even when the op-amp was not regulating. The output of the circuit (V_{out}) was the voltage required to keep the heater at a set temperature. The heat dissipated by a given heater can be directly obtained from this voltage and the heater resistance.

Sixteen of these circuits were constructed on a single card. Six of these cards plug into a motherboard that routed the signals from the host computer to the individual feedback circuits. The reader is referred to Bae, et al. (1999) for additional details regarding the circuit.

2.3 Heater Calibration

The heater array was calibrated in an insulated, circulating constant temperature oil bath that was held within 0.2 °C of the calibration temperature. Calibration consisted of finding the digital potentiometer wiper position that caused the feedback loop to just begin regulating for a given bath temperature. The uncertainty in threshold wiper position was 1 position, or about 0.34 °C in heater temperature.
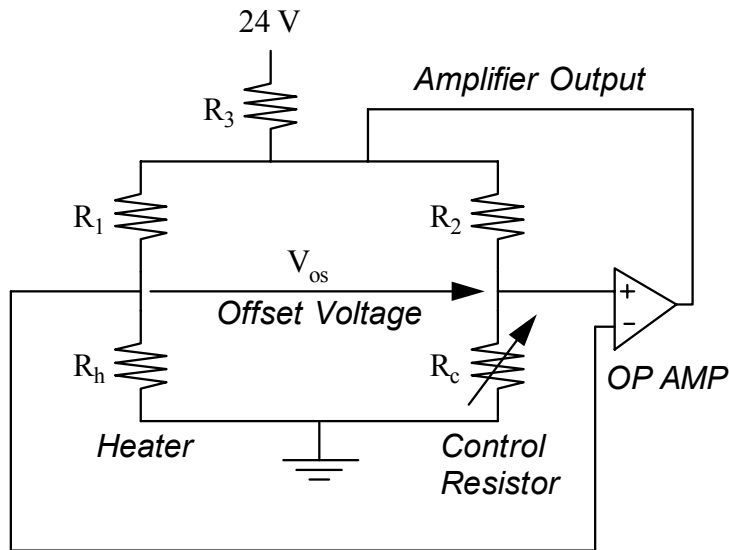
Figure 2.2: Schematic of electronic feedback loop in heater element.

2.4 Test Conditions, Set Up and Data Acquisition Systems

A schematic of the test apparatus is shown in Figure 2.3. The drops were produced by allowing fluid to drip from a glass nozzle onto the heater array. The working fluid used in this study was PF-5060, which effectively replaces CFC-113 as a dielectric coolant. No effort was made to degas the liquid prior to use.

Three sets of experiments were conducted with the heater array set at temperatures of 85 °C, 75 °C, and 65 °C. The release height of the droplets was kept constant, and all of the droplets pinched off from the glass nozzle with a nominal diameter of 0.82 mm and impacted the heater array with a nominal velocity of 0.3 m/s. A summary of the droplet initial conditions is shown in Table 2.1.

The semi-transparent nature of the heater array enabled images to be made of the droplets evaporating on the surface from below using a High-Speed CCD camera (Vision Research Phantom 500 V 3.0) set at 500 fps and 512 × 512 resolution with a 3.5X tele/microscope lens (Infinity Model KC lens with IF4 objective). Pictures were also taken from the side using another high-speed digital video camera (Kodak Motion Corder Analyzer SR Ultra), set at 512 × 480 resolution and 250 fps and a second microscope lens (Infinity model K2, with STD objective). Recording was initiated using the same trigger signal sent to the data acquisition system, allowing heat transfer measurements to be synchronized with the high-speed images. The side-view images were used to calculate the initial diameter of the droplet, the impact
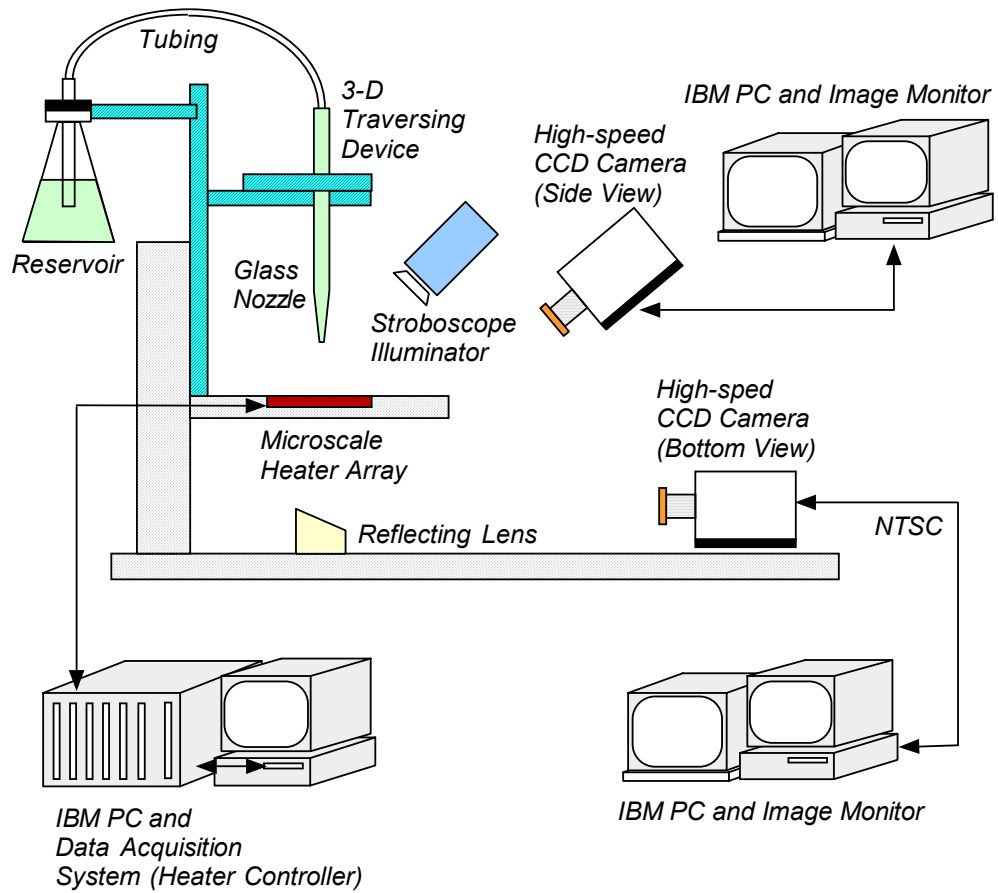
Figure 2.3: Schematic of experimental apparatus.

Table 2.1: Experimental parameters in this study.

Heater Temperature [^{o}C]	Droplet Diameter [mm]	Droplet Velocity [m/s]	Weber Number	Reynolds Number
85	0.82	0.31	10.8	629
75	0.83	0.32	11.6	657
65	0.82	0.31	11.1	635

velocity, and the contact angle during the evaporation process. The impact velocity was calculated by measuring the droplet displacement between successive frames from the high-speed images. The diameter of the splat was measured from both the side-view and the bottom-view of the heater array. Based upon the resolution and depth-of-focus of the images, the uncertainty in the initial drop size and impact velocity is approximately 5%. The data acquisition system consisted of two A/D boards (ComputerBoards CIO-DAS6402-12) installed in a PC, and was capable of sampling the output of each heater at speeds up to 3.3 kHz with 12 bits of resolution. This system was used to obtain time-resolved data at 3000 samples/sec from each heater for 5.0 seconds. Data acquisition was triggered by the rising edge of a TTL signal from the computer and data was stored to disk.

2.5. Data Reduction and Uncertainty Analysis

The instantaneous power required to keep each heater at a constant temperature was measured and used to determine the heat flux from each heater element. Because all the heaters in the array were at essentially the same temperature, heat conduction between adjacent heaters was negligible. The total heat flux measured for each heater (q''_{raw}), however, needed to be corrected to account for substrate conduction. q''_{raw} could be lost through the bottom by conduction through the substrate (q''_{sc}), through the top by natural convection to the air before droplet impacts (q''_{nc}), or into the liquid after droplet impact (q''_{liq}). In all of the cases studied, q''_{nc} was much smaller than either q''_{sc} or q''_{liq} and could be neglected. Before the droplet impacted the heater array, the power supplied to each heater was lost only by substrate conduction. Because the heaters were held at constant temperature, the substrate conduction remained constant even after droplet impact, enabling the heat transferred from the heaters to the liquid to be determined by subtracting q''_{sc} from q''_{raw}.

The uncertainty in the final heat flux values resulted from uncertainties in q''_{raw}, q''_{nc}, and q''_{sc}. Uncertainties in q''_{raw} were relatively small since they were computed directly from the measured voltage across the heaters and since the heater resistances did not change much. The maximum uncertainty in the voltage across the heater was 0.02 V. The uncertainty in heater resistance was

about 1 Ω. Since the heater resistance was nominally 750 Ω, the % uncertainty in heater resistance was about 0.14 %.

The uncertainty of the local heat flux measurements was estimated for a typical heater voltage of 2 V using the method suggested by Kline and McClintock (1953). The estimated uncertainty in q''_{raw} was about 2 %. The uncertainties in q''_{nc} and q''_{sc} were estimated to be about 5 % and 2 %, respectively. The uncertainty in q''_{nc} could be large, but it contributed very little to the final uncertainty, since the actual value of q''_{nc} was very small compared to q''_{sc} (q''_{nc} was about 5 % of that of q''_{sc}). The final uncertainty in the heat flux was therefore small compared to the uncertainty in droplet diameters (4 %). The uncertainty in droplet diameter translated into a much larger uncertainty when computing the energy required to evaporate the drop because of the dependence on d_o^3.

3. RESULTS AND DISCUSSION

3.1 Droplet Heat Transfer and Comparison with Droplet Evaporation Model

3.1.1 Droplet Flow Visualization

Time resolved evolution of the droplet deformation viewed from beneath the heater array with the heaters set at 65 ^{o}C are shown on Figure 3.1. The droplet reaches its maximum diameter at approximately $t = 4$ ms, after which the droplet recoils and reaches a minimum diameter at $t = 10$ ms. The cycle repeats several times until the motion is sufficiently damped by viscosity around 30 ms.

Snapshots of the drop at three superheats 100 ms after impact is shown on Figure 3.2. At the highest superheat (85 °C), boiling within the drop is though to occur. At the two lower superheats, bubbles within the drops were seen, but it is thought that these are due to dissolved gas coming out of solution. These observations are supported by additional evidence from the transient heat flux measurements to be discussed below.

3.1.2 Contact angle and wetting parameter

The time-resolved variation in the liquid-solid contact angle θ is shown in Figure 3.3a. The uncertainty in the measurement of contact angles is $\pm$ 5°, while the uncertainty in contact diameter is $\pm$ 0.03 mm. The contact angle is seen to change with temperature. Large contact angles for the 85 °C case were expected since boiling within the droplet caused its volume to increase. The contact angles for the 75 °C case might be larger than those for the 65 °C case due to more boiling within the drop.

3.1.3 Energy balance

The energy transferred from the wall to the drop can be obtained by integrating the measured wall heat transfer over all the heaters and the entire droplet evaporation time:

$$Q = \sum_{t=0}^{t=t_e} \sum_{i=1}^{i=N} q_i''(t) A_i \Delta t \tag{11}$$

This energy can be converted into an equivalent droplet diameter (d_{eq}) using an energy balance on the drop

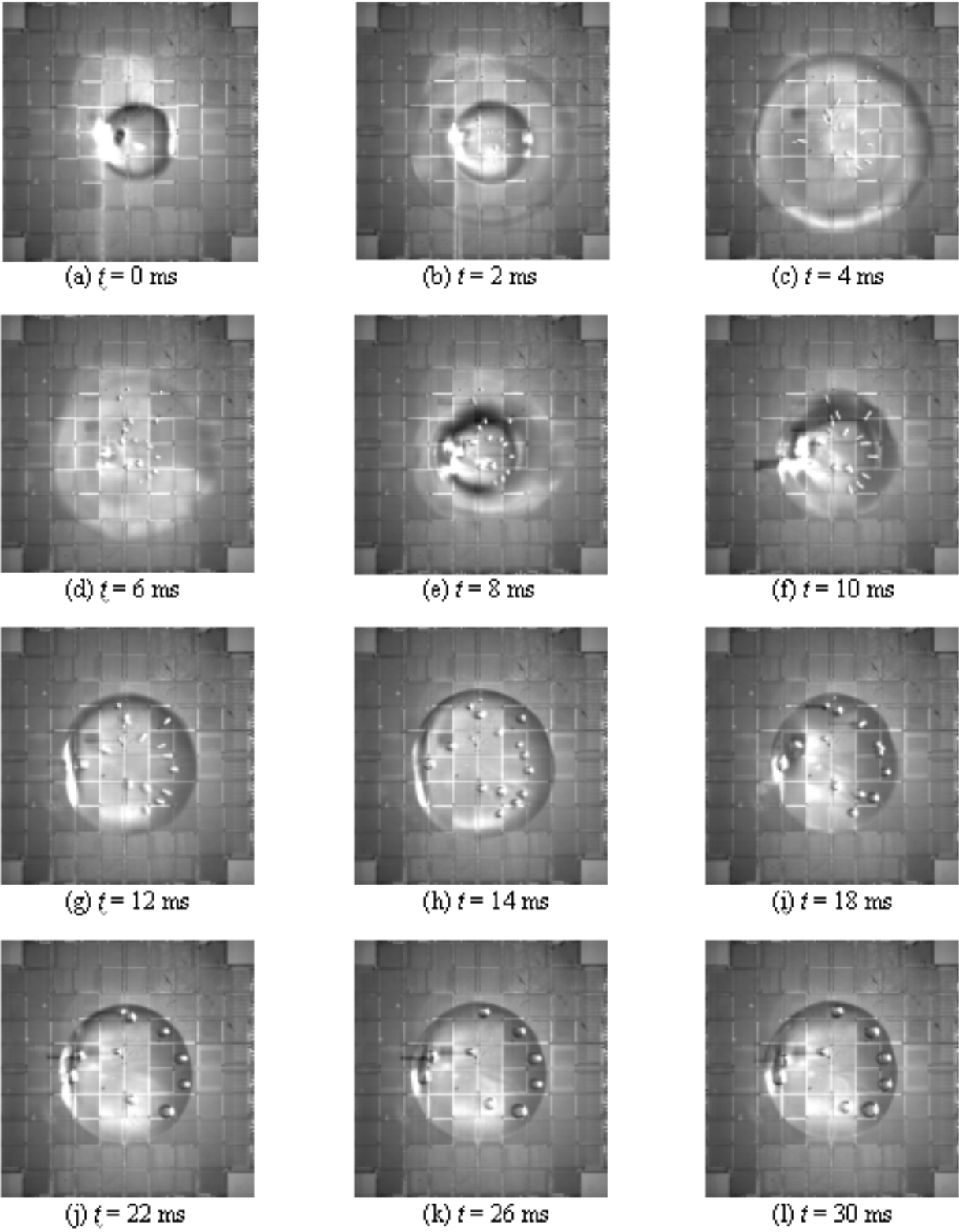(a) $t = 0$ ms

(b) $t = 2$ ms

(c) $t = 4$ ms

(d) $t = 6$ ms

(e) $t = 8$ ms

(f) $t = 10$ ms

(g) $t = 12$ ms

(h) $t = 14$ ms

(i) $t = 18$ ms

(j) $t = 22$ ms

(k) $t = 26$ ms

(l) $t = 30$ ms

Figure 3.1: Time resolved images of droplet impact.

(a) 85 °C   (b) 75 °C   (c) 65 °C
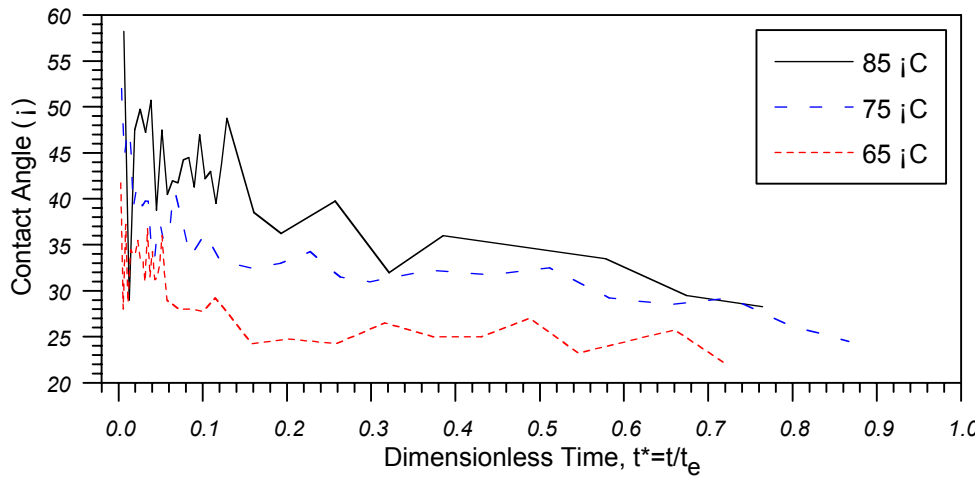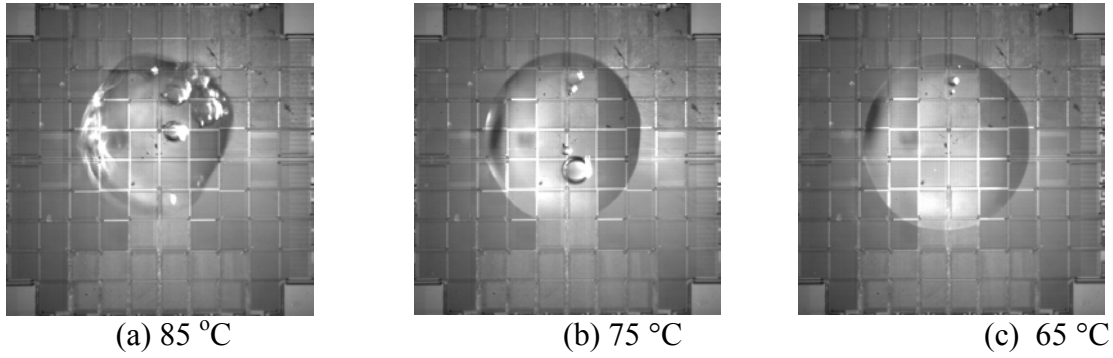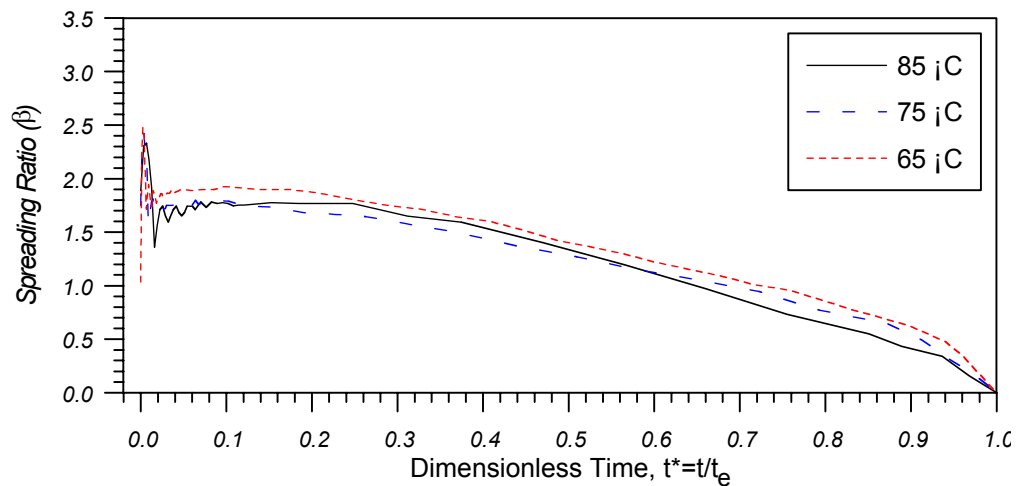

Figure 3.2. Droplets at 85 °C, 75 °C, and 65 °C at 100 ms.

(a) Liquid-solid contact angle, θ

(b) Spreading Ratio, β

Figure 3.3.   Variations in time-resolved liquid-solid contact angle and spreading ratio after impact, normalized on droplet evaporation time.

$$Q = \rho_d \pi \frac{d_{eq}^6}{6} \left[c_p \left(T_{sat} - T_0 \right) + h_{fg} \right] \tag{12}$$

Shown on Table 3.1 is the ratio of d_o to d_{eq}. This ratio is very close to unity, suggesting that the measurements are accurate. d_{eq} is seen to be slightly larger than d_o, which is impossible, but the discrepancy could easily be due to improper fluid property values and/or errors in measuring the droplet diameter. In fact, the uncertainty in droplet diameter alone accounts for much of the discrepancy.

3.1.4 Time resolved heat flux

The time-resolved heat transfer variation from the array at the three superheats is shown in Figure 3.4. The ordinate was obtained using the following equation:

$$q(t) = \sum_{i=1}^{i=N} q_i''(t) A_i \tag{13}$$

where $q_i''(t)$ is the wall heat flux at time t for heater i corrected for substrate conduction. It is seen that the droplet evaporation time decreases with increasing wall temperature, as would be expected. The heat rate $q(t)$ trace for a wall temperature of 85 °C contains a high-frequency component from droplet impact to about 0.42 s. Correlation with the high-speed video indicated that this activity was due to nucleate boiling within the splat. Very few bubbles were observed after 0.42 s at this superheat. After 0.42 s, the heat transfer suddenly decreased, indicating the end of boiling. The minimum film thickness to support nucleate boiling was theoretically suggested by Chen et al. (1977):

$$\delta_{min} = \frac{8 \sigma T_{sat}}{\rho_v h_{fg} \left(T_w - T_{sat} \right)} \tag{14}$$

Using the properties of PF-5060 with a wall temperature of 85 C, equation (14) gives a value of 1 μm for the minimum thickness to support boiling. Estimating the remaining drop volume at this time using the amount of energy transferred to the droplet reveals that approximately 10 % of the original droplet volume remained, giving an average splat thickness of 85 μm. The source of this discrepancy is currently not understood. The droplet behavior at this superheat could be classified as belonging to the intermediate superheat regime. The heat flux traces for wall temperatures of 75 °C and 65 °C do not contain any high-frequency activity, indicating little boiling within the splat–this behavior is consistent with droplet evaporation in the low superheat

Table 3.1: Droplet energy balance.

T_w [°C]	t_e [s]	Q_{meas} [J]	d [mm]	d_{eq} [mm]	d / d_{eq}
85	0.63	0.069	0.82	0.87	**95 %**
75	1.13	0.062	0.83	0.84	**99 %**
65	1.55	0.061	0.82	0.83	**98 %**
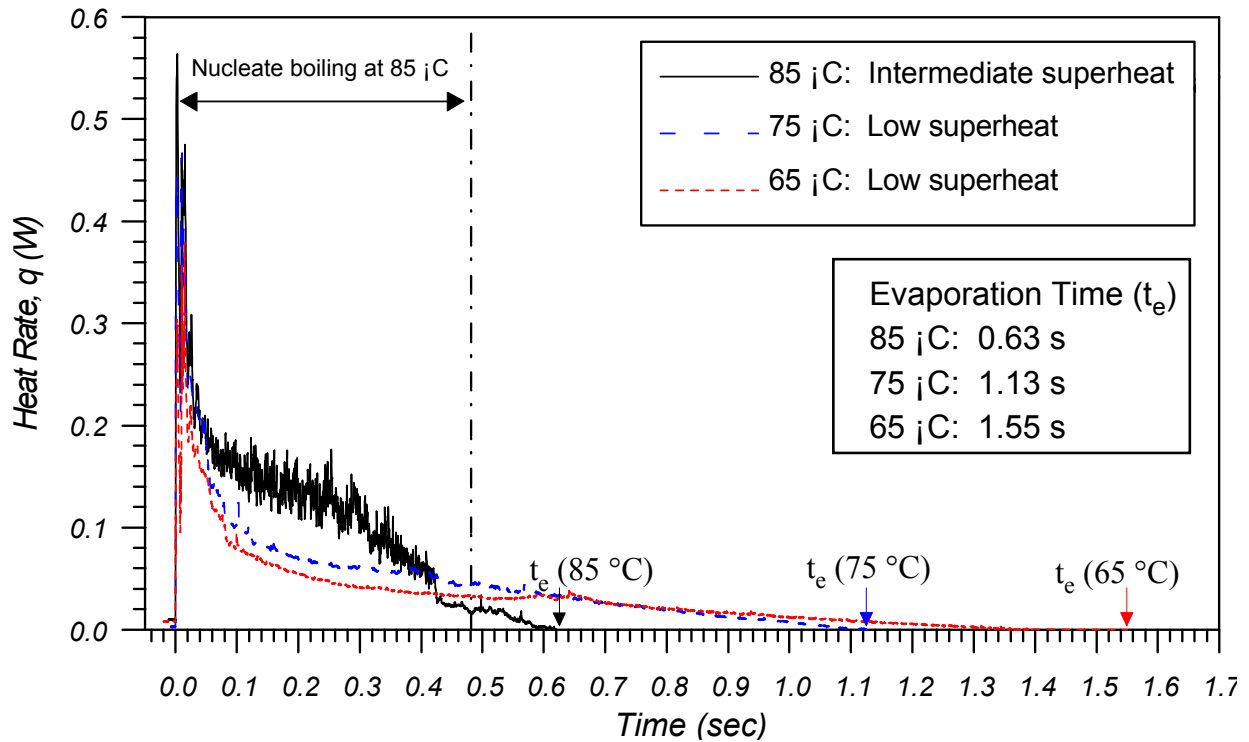
Figure 3.4. Time-resolved distributions in rate of heat with $T_w = 85$, 75, and 65 °C.

regime.

    The time-resolved heat transfer distributions along with β shortly after impact ($0 < t < 100$ ms) is shown in Figure 3.5. The data is seen to be remarkably repeatable from drop to drop at all temperatures. For $0 < t < 20$ ms, the tested data show oscillations in the heat flux level whose peaks and valleys correspond with the oscillations in the spread ratio, β.

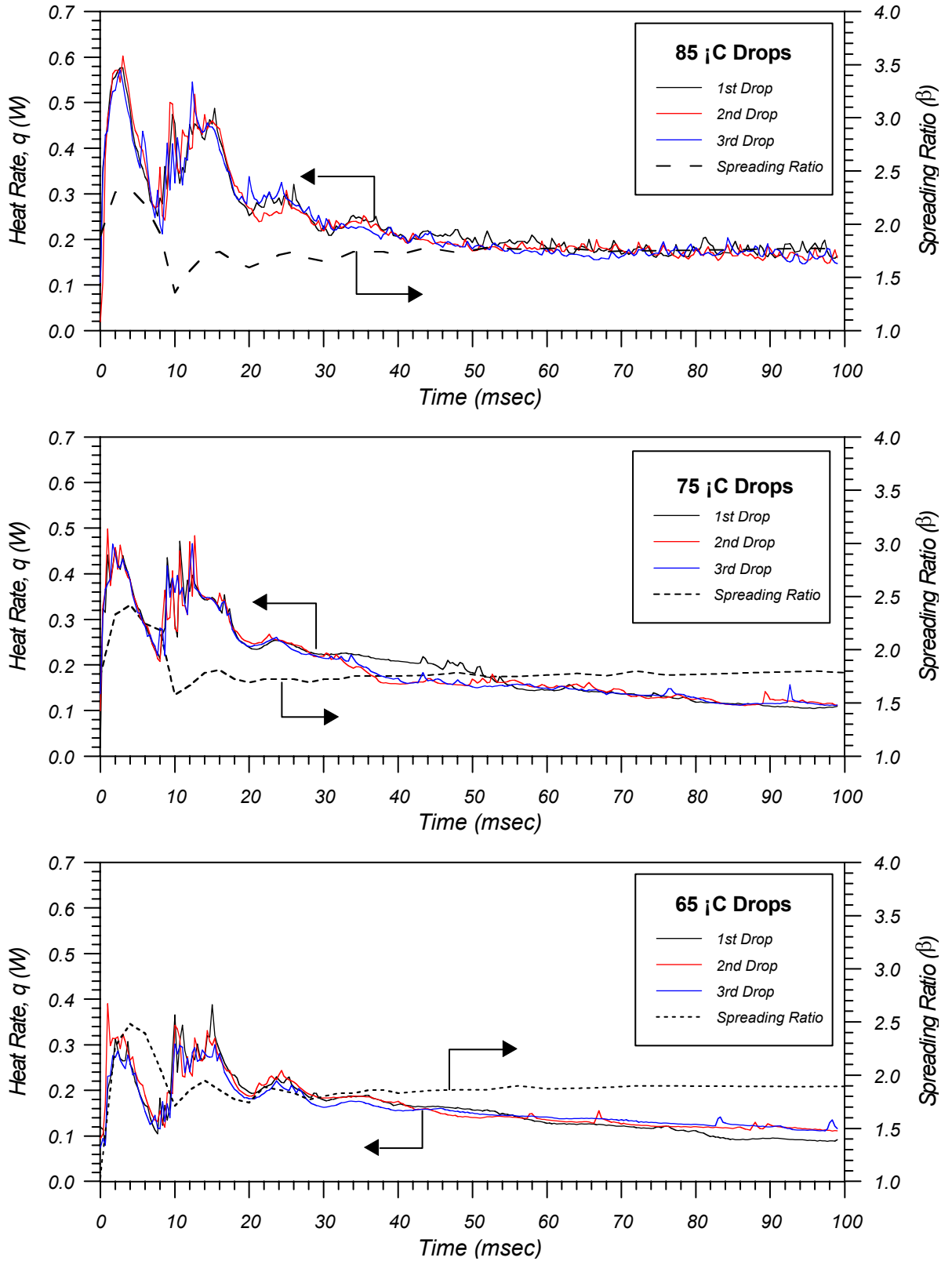**Figure 3.5. Time-resolved heat rate distributions after impact for 0.1 sec (T_w = 85, 75, and 65 ^{o}C).**
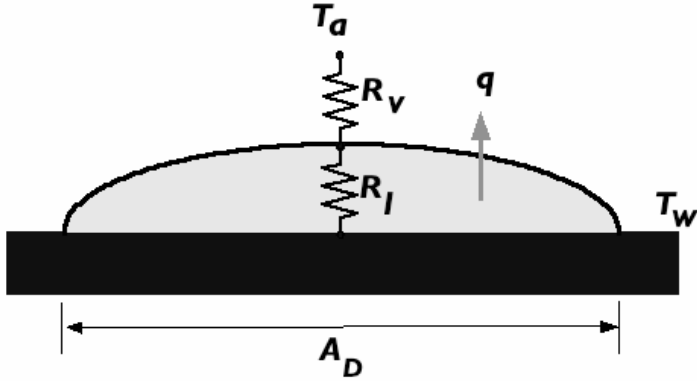
Figure 3.6. Droplet resistance schematic.

3.1.5 Droplet Thermal Resistance

The droplet heat transfer is determined by the thermal resistance within the droplet ($R_l = \delta/kA_D$) and the resistance associated with vapor removal from the top of the droplet ($R_v = 1/h_vA_D$) as indicated on Figure 3.6. The total heat transfer coefficient (h) is related to the thermal resistances by

$$R_{th} = R_l + R_v = \frac{1}{hA_D} \tag{15}$$

As a droplet evaporates, R_l decreases since the thickness of the splat decreases. Just before the final liquid evaporates, the total thermal resistance is dominated by R_v.

The variation in heat transfer coefficient with time can be computed using the data from Eq. (1). In terms of the droplet variables, h is given by

$$h(t) = \frac{4}{(T_w - T_a)} \frac{q(t)}{\pi d_0^2 \beta(t)^2} \tag{16}$$

Plots of the variation in $h(t)$ is shown on Figure 3.7. It is seen that h is relatively constant for $0.2 < t^* < 1.0$ for all three wall temperatures. The significance of a constant h over this period is that it indicates that thermal resistance within the liquid is negligible compared to the thermal resistance associated with vapor removal. If the thermal resistance in the liquid was important, then a rise in h should have been observed as the droplet evaporates since R_l decreases as the droplet thins. The results show that in order to increase the heat transfer coefficient, one must increase the rate at which vapor is removed from the top of the drop, consistent with the findings of Qiao and Chandra (1997), di Marzo and Evans (1989), and di Marzo et al. (1993).
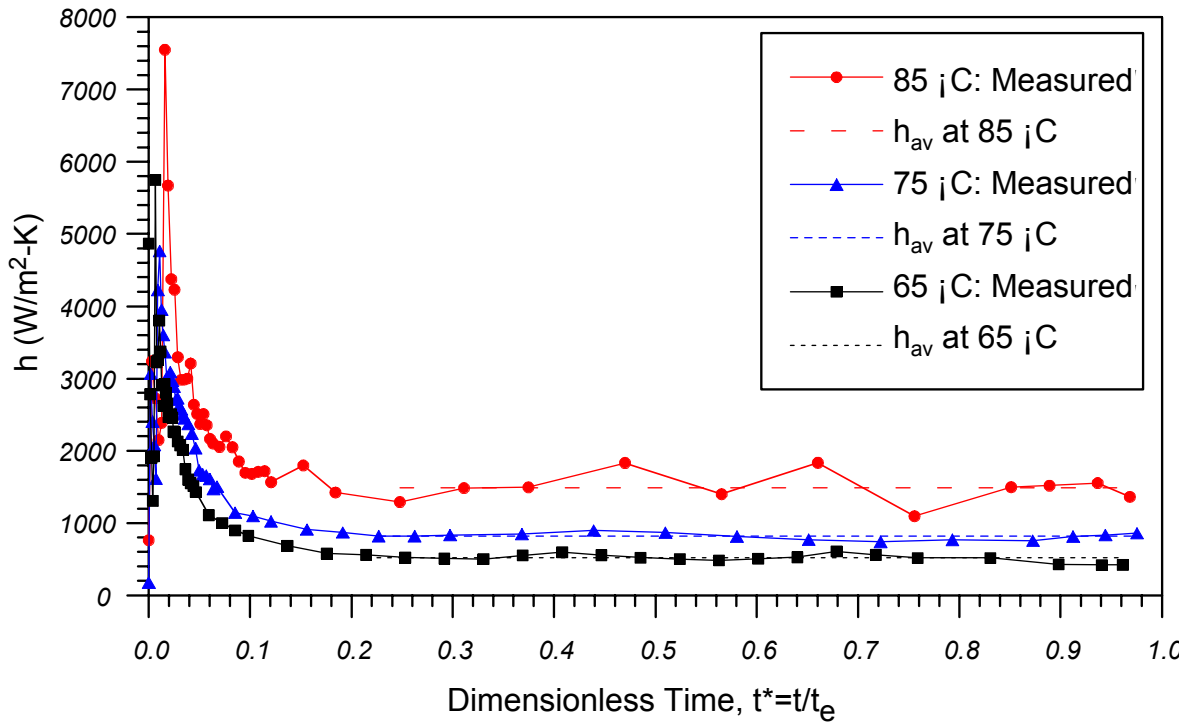
20

Figure 3.7. Time-resolved heat transfer coefficient (*h*) during evaporation time, *t$_e$*, and average heat transfer coefficient (*h$_{av}$*) at *T$_w$* = 85, 75, and 65 °C.

For $0 < t^* < 0.2$, however, a transient spike in the value of *h* is observed (see Figure 3.8). It is of interest to note that the transients all appear to collapse onto the same curve when plotted against dimensional time, indicating that the early evolution of *h* depends linearly on the temperature difference, and does not depend on the total evaporation time of the droplet. Several possible mechanisms may be responsible for this behavior. First, this behavior might be caused by transient conduction heating of the droplet from its original ambient temperature to its saturation temperature. This can be checked by approximating the droplet as a semi-infinite solid that is suddenly subject to a step change in wall temperature, and calculating the transient heat flux that would occur across its boundary. If one assumes the mass transfer effects to be relatively weak at the ambient temperatures, then the solution should remain valid until the heat wave just begins to reach the outer surface of the drop and starts to increase the temperature of the gas/liquid interface above the initial value *T$_o$*. Using the properties of PF-5060, the transient heat transfer coefficient for such conditions are plotted in Figure 3.8. Assuming the droplet to be a disk of uniform thickness consistent with the initial droplet volume and contact area, the time
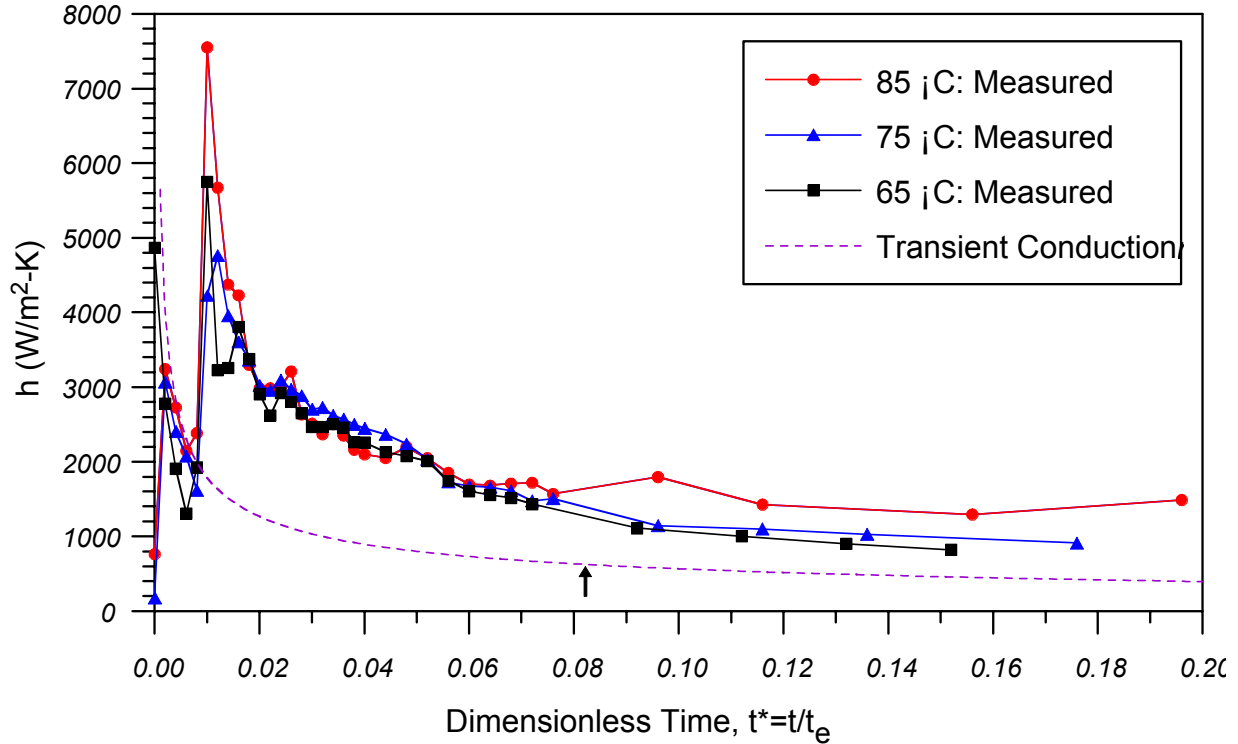
Figure 3.8. Detail view of heat transfer coefficient.

at which the heat wave first reaches the upper surface of the hypothetical splat is indicated by the arrow (assumed to occur when the surface temperature has increased by 2 % of the initial temperature difference). From this result, one sees a qualitative agreement during the first 6 to 8 ms when the droplet initially contacts the surface. After 8 ms, however, the heat transfer coefficient increases sharply, and resumes a more gradual decay with a few minor oscillations before reaching its steady-state value at $t = 150$ ms. The second sharp increase in h corresponds to a time during which the heat flux is rapidly rising, but β is still rapidly decreasing (see Figure 3.5, between 8 and 12 ms). Although the transient conduction profile tracks the general shape of the second decay event, the actual decay event is obviously complicated by additional effects such as the oscillatory motion within the drop.

A second possible cause for the variation in h may reflect a change in R_v due to a change in the concentration gradient at the liquid/vapor interface. Vapor removal from the top of the drop occurs primarily by diffusion in this experiment since there was little air movement over the drop. When the drop first impacts the surface, rapid vapor removal occurs since the

22

concentration gradient is steep. As liquid evaporates, however, the concentration boundary layer thickens, decreasing the concentration gradient and therefore the vapor removal rate.

Third, bubbles within the drop that occur due to degassing of the fluid might have the effect of increasing the surface area at the top of the drop, allowing vapor to leave the surface more readily, thus decreasing R_{th} and increasing h. As degassing of the fluid occurs, the bubble size decreases along with the surface area, resulting in a decrease in h.

Future models need to include such effects to accurately capture the early history of the evaporation transient. Qiao and Chandra (1997), di Marzo and Evans (1989), and di Marzo et al. (1993) did not observe these strong transients in h during the first stage of evaporation, probably because the drops in their studies took much longer to evaporate than those in this study.

3.1.6 Comparison to Two Stage Model

The nonuniform heat transfer coefficient observed during the first stage of the evaporation process indicates that the first stage evaporation model cannot be applied to these droplets. As shown in Figure 3.7, the assumption in constant heat transfer coefficient h can be applied only at the second stage, proposed by di Marzo and Evans (1989), diMarzo et al. (1993), and Qiao and Chandra (1997). During the second stage, the calculated heat transfer coefficient h_{cal} can be estimated from Eq. (4) assuming $t_e = t_{e2}$ and V_o equal to the volume of the droplet at the beginning of the second stage (computed using Eq. (3) with $\theta = \theta_r$ and D equal to the splat diameter at the beginning of the second stage). The average drop area A_{av} is equal to the average splat area during the second stage ($A_{av,2}$):

$$A_{av,2} = \frac{1}{t_{e2}} \int_{t_{e1}}^{t_e} \frac{\pi}{4} d_0^2 \beta^2 (t) dt \tag{17}$$

Comparison of the calculated value h_{cal} is made with the measured value h_{av} on Table 3.2. Very good agreement is observed, indicating that the second stage model is quite accurate.

For the second stage of evaporation, the rate of change in splat diameter during the second stage can be computed using Eq. (9). Comparison to the data can be performed by drawing a line with the slope given by Eq. (9) through a data point in the middle of the second stage as seen on Figure 3.9. The value of θ_r and h_{av} used in the computation was the average between $0.2 < t^*$ < 1.0 in Figures 7 and 11 respectively. The good agreement between the computed line and the

data indicates that the second stage model predicts quite well the variation in splat diameter with time during the droplet evaporation process.

Table 3.2. Comparison between calculated and measured average heat transfer coefficient.

T_w [°C]	h_{av} [W/m²·°C]	h_{cal} [W/m²·°C]	h_{av} / h_{cal}
85	1,488	1,498	**99 %**
75	814	822	**99 %**
65	515	523	**98 %**

Table 3.3. Comparison between estimated and measured second evaporation time.

T_w [°C]	$t_{e2, meas}$ [second]	$t_{e2, cal}$ [second]	$t_{e2, meas} / t_{e2, cal}$
85	0.47	0.58	**81 %**
75	0.85	1.09	**78 %**
65	1.16	1.62	**72 %**

The second stage evaporation time t_{e2} can be predicted using Eq. (10) for known values of D_o, h_{av}, and θ_r. The estimated values of t_{e2} are compared with the measured values on Table 3.3. It is seen that the measured values are somewhat smaller than predicted. The discrepancy is probably due to the rapid decrease in the splat diameter towards the end of the evaporation time as seen in Figure 3.9. The reason for this is currently not known.
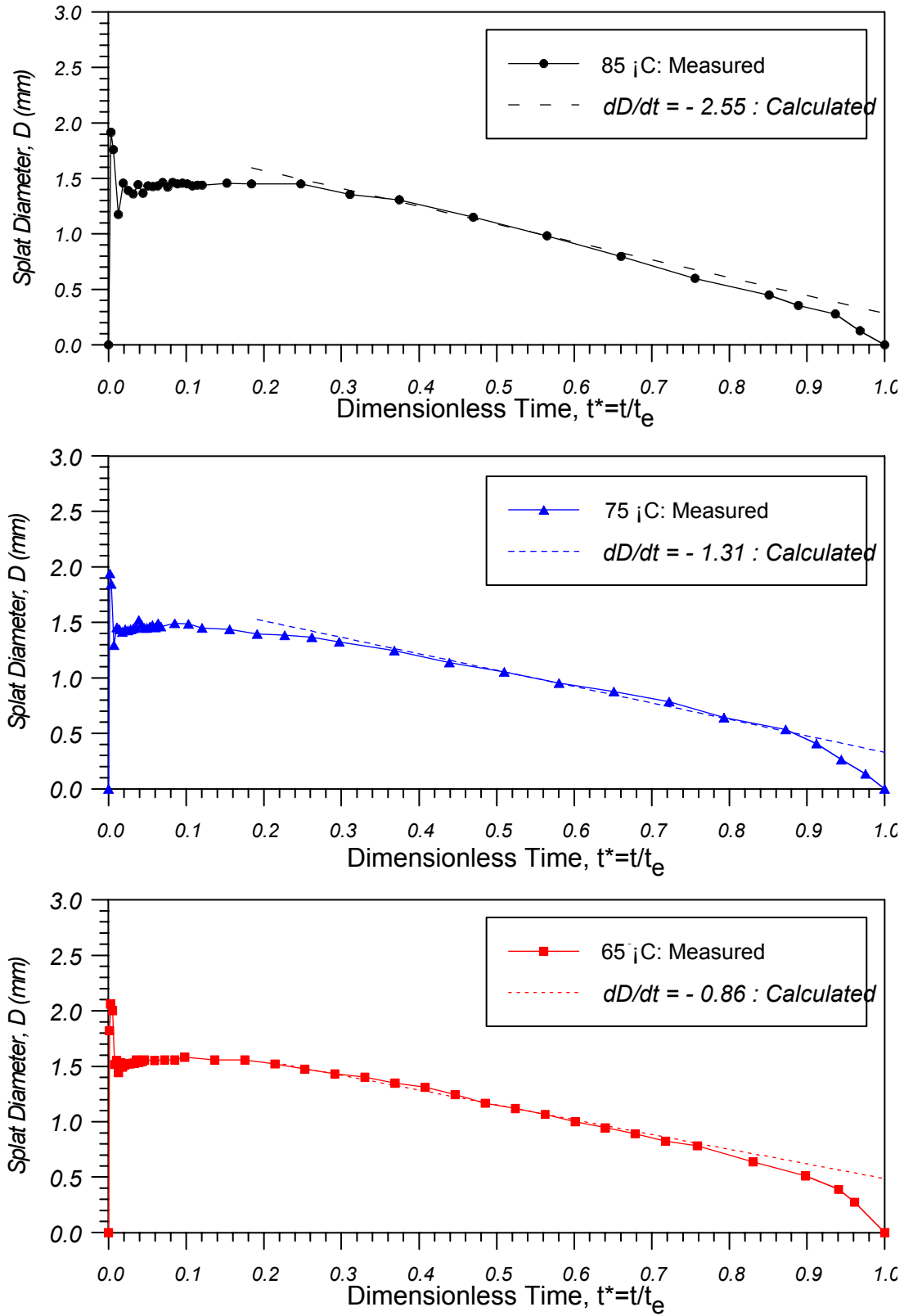
Figure 3.9. Comparison between model and measured splat diameter in second stage.

25

3.2 Effect of Dissolved Gas

A summary of the four droplet studied is given in Table 3.4. While all of the drops had dissolved gas, the gas in two of the droplet burst early, resulting in droplet evaporation similar to that discussed above. The gas in two of the other droplets, however, coalesced and formed a large primary bubble which altered the heat transfer. The difference caused by the formation of this primary bubble is discussed below.

3.2.1 Droplet Flow Visualization

Images of the droplet behavior recorded using the bottom and side-view high-speed cameras are shown in Figures 3.10-3.12. These images revealed that the droplets had a nominally similar initial history during the first 0.05 seconds, which was characterized by: 1) two to three oscillations in drop shape and surface area caused by the drop's impact on the substrate before being damped out by viscous dissipation, and 2) the formation of numerous small bubbles, which successively grew, burst, and/or coalesced. After this early stage of the drop vaporization, the process then evolved according to one of two scenarios that result in a significant difference in the total lifetime of the droplet. In the first mode, all of the smaller bubbles that were formed shortly after impact burst, leaving the liquid drop free of voids. Case T65_1 is typical of these droplets, and several selected images from this case are shown in Figure 3.10. In the initial spreading of the drop, as many as 20 to 30 small bubbles about 50 mm in diameter form and rapidly burst or coalesce in the first 15 ms. By 0.022 s, only five bubbles remain, which have now grown to approximately 150 to 200 mm in diameter. These bubbles then remain in the droplet and continue to grow, until they also burst during attempted coalescence at $t = 0.08$ s past the initial drop impact. It appears that the disturbance generated by the bursting of one pair of bubbles destabilized the last remaining pair, which finally burst about 0.084 s after impact. The oscillations caused by these bursting events are damped by $t = 0.1$ s, and the droplet assumed an approximately spherical cap shape for the remainder of its lifetime.

In the second mode of droplet vaporization, the smaller initial bubbles coalesce into a single primary bubble that survives and grows through a significant portion of the drop lifetime. Cases T65_4b and case T65_6 are examples of two drops that exhibited this behavior, and select images from their evolution are shown in Figures 3.11 and 3.12. For case T65_4b (Figure 3.11), a single bubble has survived the cascade of rupture events that occur between t=0.075 s to 0.080

Table 3.4: Summary of droplet initial conditions and evaporation times for four drops.

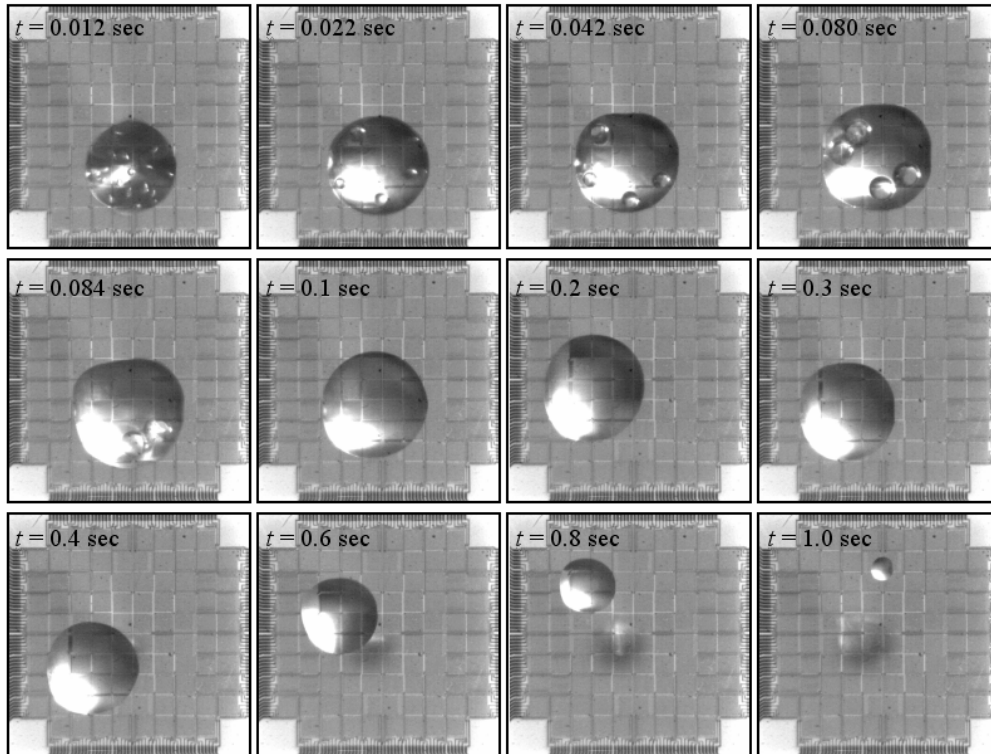| Case	Droplet diameter, D (mm)	Droplet evaporation time, t_{ev} (s)	Comments
T65_1	0.82	1.01	No primary bubble
T65_2	0.82	1.02	No primary bubble
T65_4_b	0.82	0.884	Primary bubble bursting at 0.484 s
T65_6	0.82	0.75	Primary bubble bursting at 0.6 s

Figure 3.10: Image sequence showing droplet evaporation for case T56_1, with no large bubble formation.

s. At t=0.2 s, this bubble has migrated toward the center of the droplet, and has already grown in size to approximately 0.5 mm in diameter. By $t = 0.3$ s, distortions are visible on the bubble that are likely film draining instabilities that result from vapor condensing on the upper inside surface of the bubble. This distortion is clearly visible when the bubble is larger than 0.5 mm, and typically undulates around the periphery of the bubble. The side-view images reveal that no
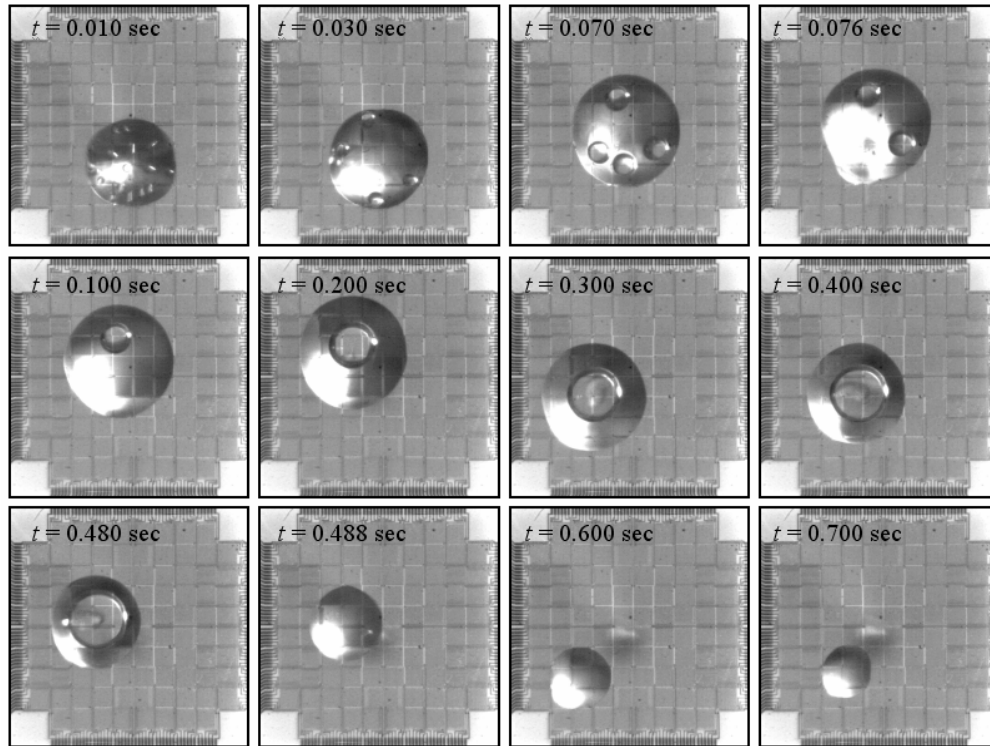
Figure 3.11: Image sequence showing droplet evaporation for case T56_4b, with large bubble formation.
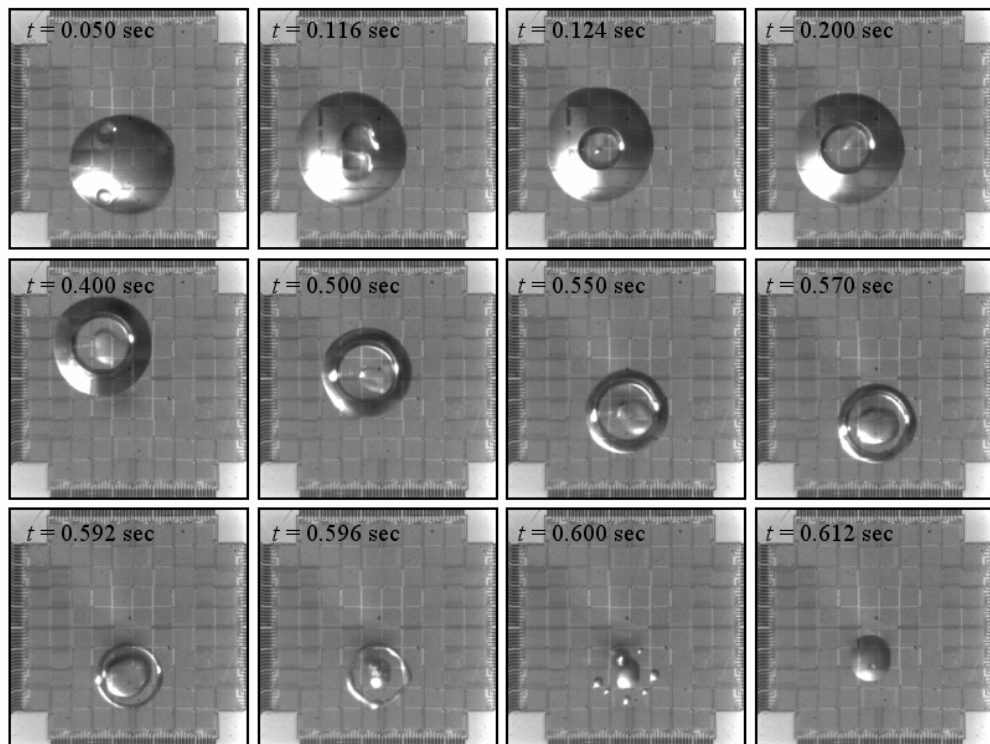

Figure 3.12: Image sequence showing droplet evaporation for case T56_6, with large bubble formation.
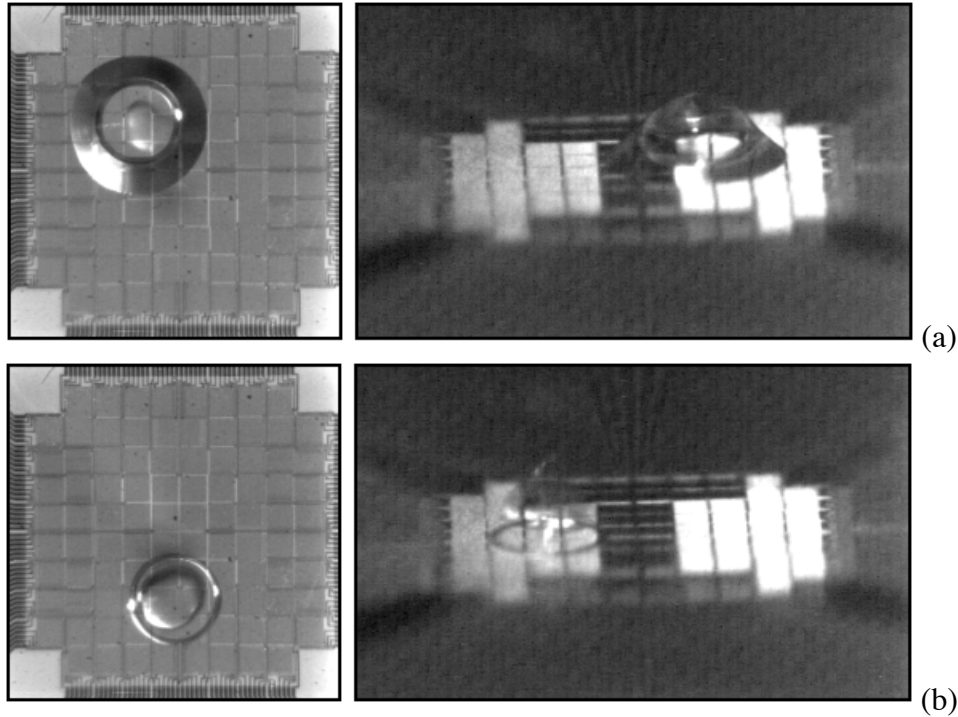
Figure 3.13: Bottom and side view of compound drop and bubble for case T56_6 at (a) $t =$ **0.400 and (b)** $t = 0.592$ **seconds. In (b), most of the liquid phase has condensed on the upper surface of the bubble, leaving it suspended by only a thin membrane above the heater surface.**

distortion is visible on the outside of the bubble, indicating that the interface is being distorted only within the bubble. Additional discussion regarding this point is given below. At $t = 0.484$ s, the primary bubble bursts, and liquid rapidly coalesces into a small spherical cap, which then evaporates according to the first mode of droplet evaporation.

The early history of drop T65_6 (Figure 3.12) is qualitatively similar to that of case T65_4b, with the exception that the primary bubble results from the coalescence of two smaller bubbles at $t = 0.116$ s, rather than the survival of an isolated bubble. An insufficient number of droplets have been examined in order to determine the factors influencing the survival or demise of the bubbles within the drop. As in the T65_4b case, the primary bubble continues to grow, and appears to have condensation and film drainage occurring inside the bubble after reaching a size of approximately 0.5 mm. Unlike the T65_4b case, the bubble survives over 0.1 s longer, resulting in a remarkable decrease in the overall lifetime of the droplet (see Table 3.4). Another interesting feature about this case is that around $t = 0.55$ s, the wetted area surrounding the

droplet appears to rapidly thin, leaving a smaller contact surface area in which to support the bubble. At the same time, the liquid film draining from the upper surface of the drop appears to temporarily stabilize, and accumulate in the form of a pendant drop within the bubble. This can be observed in the side-view images as shown in Figure 3.13 at t = 0.592 s. By t=0.594 s, the bubble has burst. Part of the pendant droplet falls down onto the heated surface and part is ejected upward, while the bubble thin film has collapsed around the base and broken into a series of smaller satellite droplets around the periphery. The part of the pendent that is ejected upward impacts onto the surface at t=0.604 s and coalesces with the portion that was previously ejected downward. Following the rapid vaporization of the satellite droplets, the remaining liquid appears to evaporate in a manner similar to the first mode of evaporation.

As a final note, no liquid was ejected outside the heated area during the bursting event of the bubbles. Although ejecta was observed during the collapse of the larger bubbles, the drops landed in the confines of the heated space for all of the results presented here. This was also confirmed from the energy balances determined from the measured heat input into the array.

3.2.2 Time resolved, space averaged heat transfer

The time-resolved heat transfer variation from the array for all of the cases are shown in Figure 3.14. The heat transfer rates shortly after impact (Figure 3.14 inset) are remarkably repeatable from drop to drop. The oscillations in heat transfer are associated with the spread and recoil of the droplet during the initial transient. The large heat transfer values are most likely associated with transient conduction and microconvection within the droplet as it heats up from room temperature.

The heat transfer curves decay at different rates after the initial transient dies out, however, with the droplet evaporation time depending mainly on the time at which the primary bubble bursts. The bubbles for cases T65_1 and T65_2 all burst by t= 0.1 s, after which the heat transfer varies similarly with time for the remainder of the evaporation process. The heat transfer variation for the two cases in which a primary bubble forms (T65_4b and T65_6) are similar until bursting occurs for T65_4b at t=0.49 s. Case T65_4b shows a case in which the bursting of the bubble is associated with a brief spike in the wall heat transfer, followed by an abrupt decrease of almost 50%. Comparison of the curves with and without the primary bubble clearly
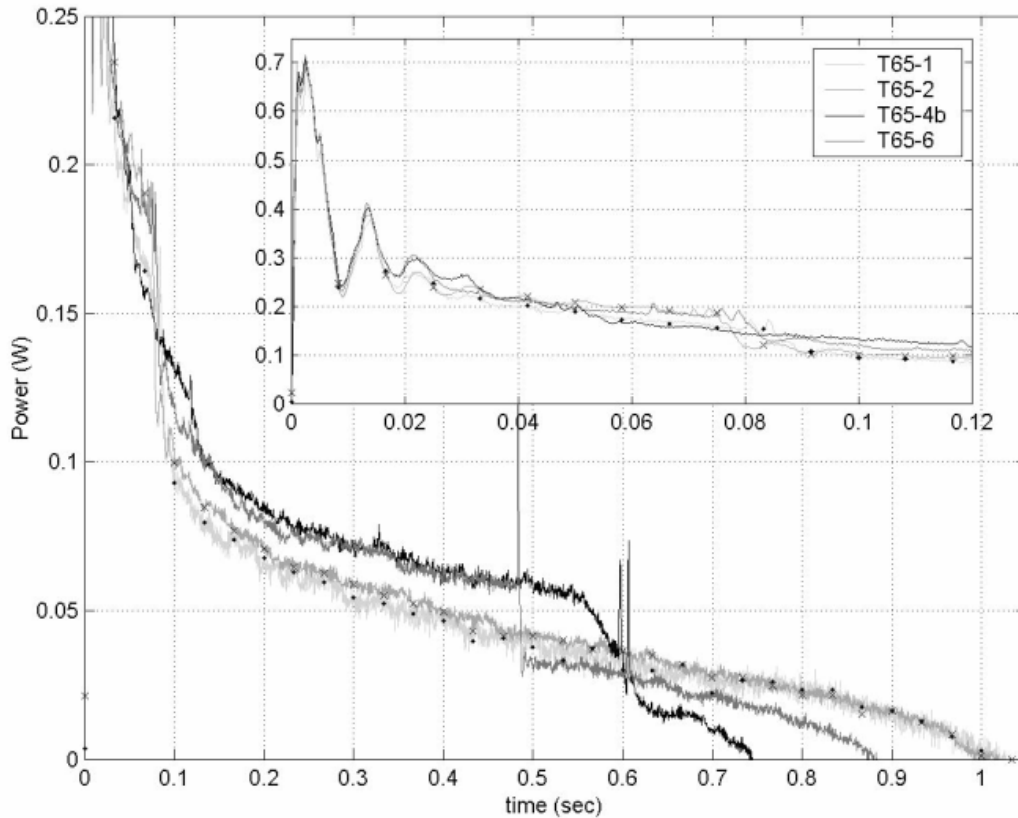
Figure 3.14: Total power dissipated to droplet as a function of time for four different cases.

indicates that the heat transfer when a primary bubble is present on the surface is higher than without the primary bubble. It is evident from energy balance considerations that this must result in a shorter droplet evaporation time. Case T65_6 shows a gradual drop in wall heat transfer between 0.55 s until the bubble burst just after 0.592 s. The reason for this behavior is discussed below. A spike in heat transfer is observed when the bubble bursts. A second spike in heat transfer centered around 0.606 s occurs when the liquid ejected upward during bubble burst impacts the surface.

There are two possible mechanisms by which a shorter evaporation time can result when a primary bubble is present. First, the bubble can cause the drop to spread out, increasing the Liquid-Solid Contact Area (LSCA) and therefore the heat transfer. Second, the bubble can increase the Liquid-Vapor Contact Area (LVCA) on top of the drop, enabling vapor to diffuse away more rapidly. Previous work by Qiao and Chandra (1997), di Marzo et al. (1993), and

Elapsed Time =   0.47   sec

a). Case T65_4b

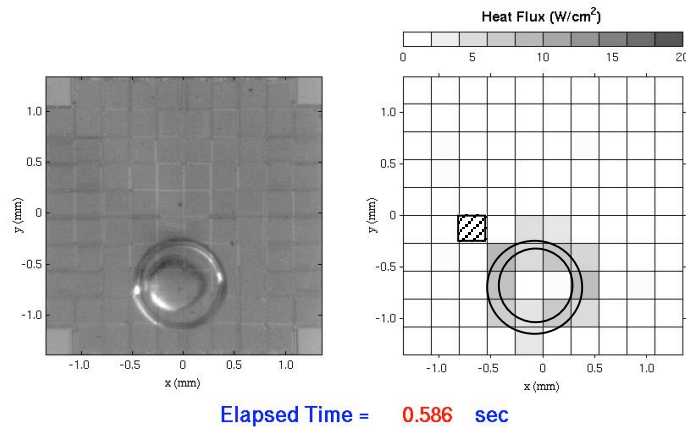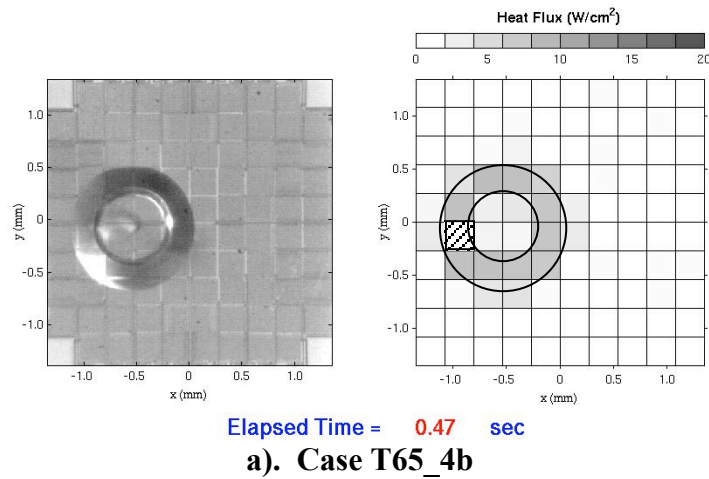Elapsed Time =   0.586   sec

b). Case T65_6

Figure 3.15: Examples of time and space resolved wall heat transfer showing low heat transfer under the primary bubble.   The cross-hatched heater is non-functional.

Milke et al. (1997) has suggested that both of these mechanisms are important, but that the limiting factor in droplet evaporation was likely the vapor removal rate.

Measurements of LSCA and LVCA were obtained from bottom and side view images, respectively, of the droplet evaporation process. The LSCA was obtained from the splat and bubble diameters. The splat diameter, D_s, was measured from the edge-to-edge distance in two orthogonal directions from the bottom view and averaged. When a primary bubble formed on the surface (Figure 3.12 and 3.13), it was assumed that a dry patch existed under the bubble. The presence of a dry patch is supported by space resolved heat transfer measurements as shown on Figure 3.15. A region of very low heat transfer is observed on the heaters that are completely enclosed within the bubble projected area. Some of the heaters are partially covered by the
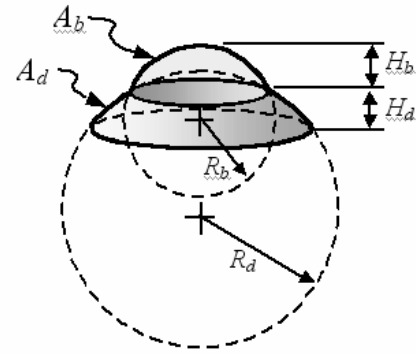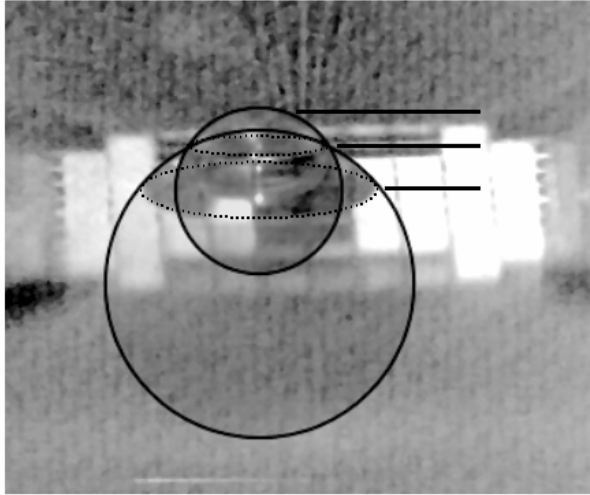
Figure 3.16: Sketch showing the measurement of the liquid-vapor surface area for compound droplet/bubble.

primary bubble, and these show a higher heat transfer. The diameter of this dry area was measured from the apparent diameter of the bubble ($D_{b,i}$), which was used to compute the LSCA as follows:

$$LSCA = \frac{\pi}{4}\left(D_s^2 - D_{b,i}^2\right)$$ (18)

The Liquid-Vapor Contact Area (LVCA) was estimated from the side view images by fitting a circle to the upper surface of the droplet, measuring the height of the droplet, and assuming that the surface had the shape of a spherical segment. For simple drops (no bubble) this area is given by (Råde & Westergren, 1995):

$$LVCA = 2\pi R_d H_d$$ (19)

where R_d is the radius of the spherical segment (which is different from the radius of the wetted liquid-solid contact area, $D_s/2$), and H_d is the height of the segment. For compound drops (cases with a single large bubble), the LVCA is estimated by assuming that both the bubble and the drop are spherical segments, and are fit with two circles; one to the bubble, and one to the liquid base drop (see Figure 3.16). Measuring the height of each segment (H_d and H_b for the drop and bubble, respectively), the LVCA is then calculated by:

$$LVCA = A_d + A_b = 2\pi\left(R_d H_d + R_b H_b\right)$$

(20)

For cases with numerous smaller bubbles, a single sphere was fit to the overall shape. Distortions caused by these bubbles, and the oscillations of the drops during the early impact history prevented the reliable estimate of the LVCA prior to $t = 0.1$ sec.

A comparison of both the LSCA ratio and the LVCA ratio to the temporal evolution of the total heat transfer rate is shown on Figure 3.17. For case T65_1, in which no bubble is present, it can be observed that both the LSCA and the LVCA (Figure 3.17a and 3.17b) remain in almost exact proportion to the heat transfer rate over most of the droplet lifetime. The exception to this is for $t < 0.2$ s, where the area ratio for the LSCA and the LVCA is distinctly below the trend for the heat transfer rate. The close agreement between the two values to the heat transfer for the drop without bubbles is not surprising–the geometry of the drop corresponds closely to a segment of a sphere during the evaporation and the minimum (receding) contact angle has been reached, fixing the proportion between the LVCA and the LSCA. This is not the case for the compound drops, however, as shown for cases T65_4b and T65_6 in Figure 3.17c-f. In these cases, the presence of the bubble increases slightly the maximum diameter of the splat as a result of the surface tension forces on the bubble. During the middle of the droplet's existence, however, the LSCA actually begins to decrease below the heat transfer curve at approximately $t = 0.35$ seconds. The LVCA, on the other hand, continues to track the heat transfer faithfully, and even matches the discontinuous jump that occurs just after the bubble bursts in case T65_4b at $t = 0.484$ seconds. For case T65_6, the LVCA also tracks quite well the gradual reduction that is induced by the growth of the primary bubble, whereas the LSCA is already 50 to 70% below the corresponding area ratio that would be required if the heat transfer were governed predominantly by the contact area with the solid surface.

3.2.3 Heat transfer coefficients

The heat transfer coefficient is given by

$$h(t) = \frac{q(t)}{A\left(T_w - T_a\right)}$$

In the present work, q(t) is measured while the temperature difference if fixed since the wall
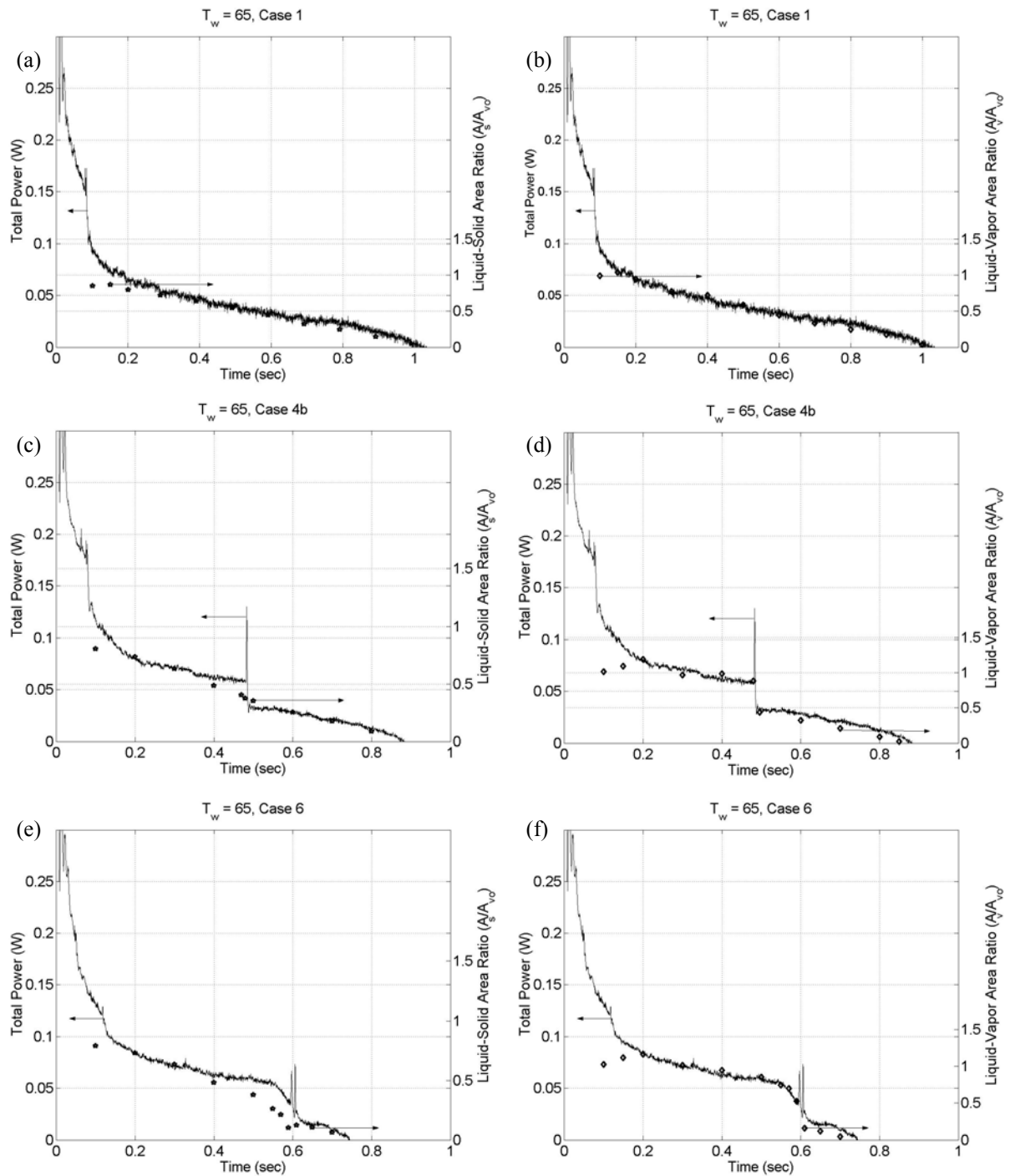
Figure 3.17: Total heat transfer rate history compared with different contact areas for different cases. (a) case 1, LSCA; (b) case 1, LVCA; (c) case 4b, LSCA; (d) case 4b, LVCA; (e) case 6, LSCA; (e) case 6, LVCA.
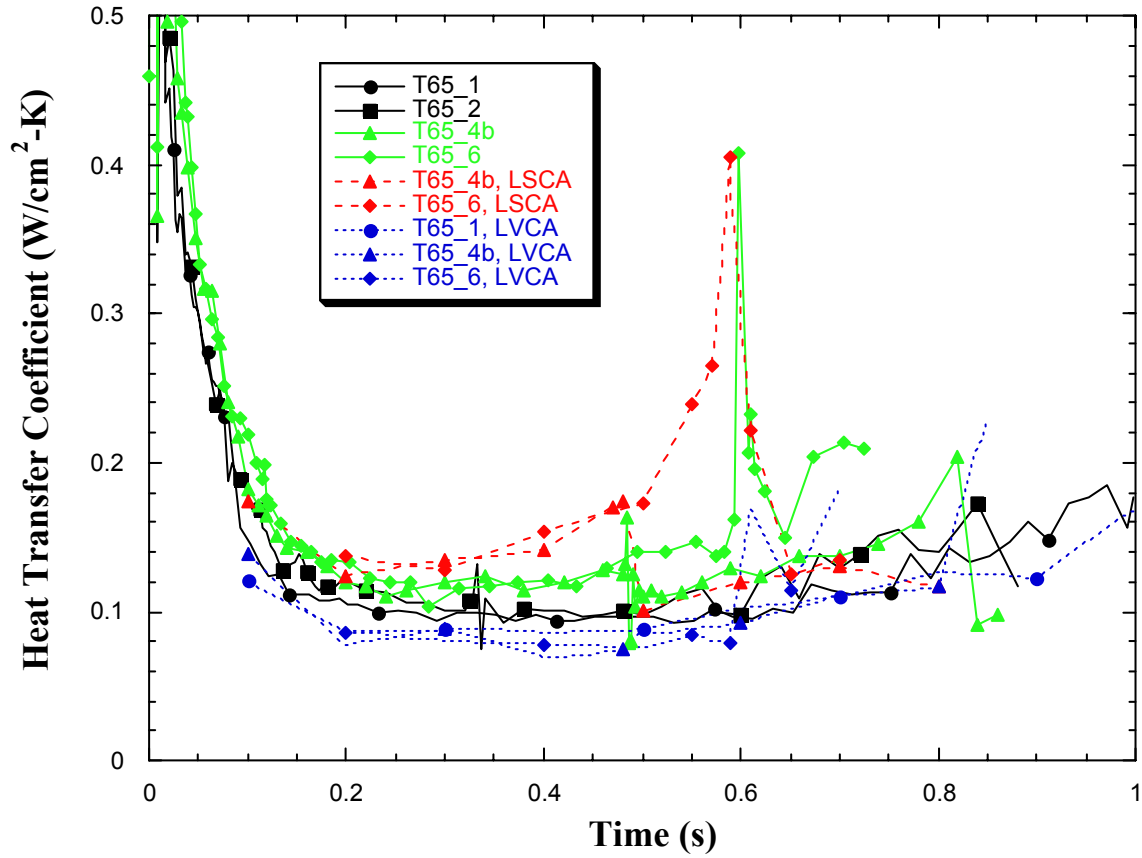
Figure 3.18: Heat transfer coefficient variation.

temperature is fixed. However, it is not obvious what the area A should be, however. Three areas that could be used are the droplet projected area (total area within the outer contact line), the LSCA, and the LVCA. Plots of the variation in *h(t)* based on these areas are shown on Figure 3.18. It can be observed that defining h(t) on the LVCA results in relatively small variations after the initial transient, particularly before and after the bubble burst. The droplet projected area and the LSCA do not faithfully track the variations in heat transfer when a primary bubble is present, as was indicated by the comparison in Figure 3.17. Defining a heat transfer coefficient based on LVCA, while not practical, does indicate that the LVCA is the controlling mechanism for droplet evaporation.

4. RECENT SPRAY COOLING MEASUREMENTS

Very little is known regarding the effects of dissolved gases on spray performance. Tilton, et al. (1992) concluded that gas degraded the condenser performance to the point where excess fluid was inhibited. They also stated that for fixed volume systems, the presence of gas would cause the boiling temperature to increase, increasing the surface temperature.   However, a recent study by Lin and Ponnappan (2002) indicated that although dissolved air degrades the performance at lower wall temperatures, the peak heat transfer is increased compared to sprays without dissolved gas. The purpose of the recent set of measurements was to clarify the role of gas on spray cooling heat transfer.

4.1 Flow Loop Description

The effects of dissolved gas and subcooling were studied using a full cone ISR spray nozzle to cool a microheater array with 0.49 cm^2 area (7.0 mm x 7.0 mm). This heater array consisted of 96 heaters each nominally 700 microns in size in the same arrangement as the 2.6 mm arrays used for the droplet cooling measurements. The tests were performed within a closed flow loop consisting of a spray chamber, condenser, and pump (see schematic on Figure 4.1) with FC-72 as the test fluid. Temperature and pressure measurements were made at the inlet to the spray nozzle and within the liquid reservoir. The pressure was observed to be uniform throughout the flow loop under all conditions tested. Liquid flow to the spray nozzle was measured using a rotometer. The heater array was inclined at a slight angle to the vertical to help excess fluid that did not drain through the condenser into the reservoir. The pump was a magnetically coupled gear pump with a head capable of pumping about 60 ml/min. The amount of dissolved gas within the liquid can be varied by controlling the pressure within the test section using a vacuum pump. A chiller consisting of a copper coil immersed in an ice bath or LN_2 bath was used in some cases to cool the liquid entering the spray nozzle.

4.2 Effect of Gas

Any gas will increase the pressure in the test section above the saturation pressure of the liquid corresponding to the reservoir temperature. Henry's law can be used to determine the
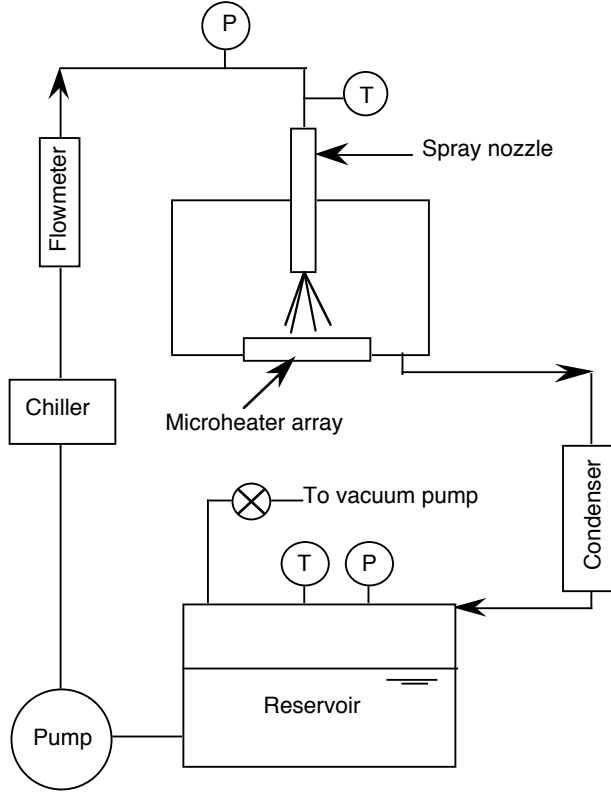
Figure 4.1: Schematic of flow loop.

amount of dissolved gas in the liquid. The dissolved gas concentration C_g (moles gas/mole liquid) in the liquid phase is given by

$$C_g = H(T)P_g$$

where P_g is the partial pressure of the gas above the liquid and $H(T)$ is Henry's constant. For air in FC-72, this has been measured to be 5.4×10^{-5} mole/mole-kPa for 31 °C<T<60 °C. P_g can be determined from a measurement of the pressure (P_{tot}) and temperature (T_{sat}) of the gas above the liquid after it has come to equilibrium in a sealed container from the following equation:

$$P_g = P_{tot} - P_{sat}(T_{sat})$$

where P_{sat} is the saturation pressure of the liquid at the measured temperature T_{sat}. The vapor pressure of FC-72 is 0.26 atm at 22 °C and 1 atm at 56.6 °C.

Subcooling of the liquid entering the spray nozzle can be accomplished in two ways. Consider first the case where all gas has been removed from the test section. The pressure in the flow loop then corresponds to the vapor pressure at the temperature of the liquid in the reservoir, and the liquid in the reservoir is at saturated conditions. Liquid can be pumped from the reservoir through a chiller to decrease its temperature before being sprayed on the heater. The liquid sprayed onto the heater is now in a state we will refer to as "thermally subcooled", and will be referenced as "TS" which is defined as the temperature difference between the reservoir temperature and the spray temperature. Consider next the case where air is allowed into the flow loop. The saturation temperature of the liquid in the reservoir has now increased since the pressure above the liquid is higher than the vapor pressure. Even if the liquid from the reservoir is not cooled before entering the spray nozzle, the liquid being sprayed onto the heater will be subcooled since its temperature is below the saturation temperature. The liquid sprayed onto the heater is in a state we will refer to as "gas subcooled" (this is similar to the terminology used by Rainey et al. (2003) in their studies of gas effects on pool boiling), and will be referenced as "GS" which is defined as the temperature difference between the saturation temperature and the reservoir temperature. The total subcooling (TotS) is defined as TotS=TS+GS.

It is seen that the effect of gas is to change the saturation temperature of the liquid, and therefore the amount by which the liquid being sprayed on the surface is subcooled for a constant spray temperature. For example, consider the case where liquid FC-72 is at 22 °C in the reservoir. If the flow loop is at 1 atm due to the presence of gas (T_{sat}=56.6 °C) and liquid from the reservoir is sprayed onto the heater, the liquid will be gas subcooled by GS=34.6 °C (=56.6-22). If the gas is now completely removed from the flow loop, the liquid spray will be saturated and the pressure in the loop will be 0.26 atm. In order to match the subcooling for the 1 atm case, the liquid will need to be thermally subcooled to –12.6 °C (=22-34.6 °C). It is also possible for TS to be negative if gas is present if the liquid heats up above the reservoir temperature in the spray nozzle. The subcooled state of the liquid being sprayed onto the heater can be characterized by specifying TS and GS.

4.3 Results

Results were obtained with the spray nozzle oriented normally to the microheater array, and 16 mm from the surface. All of the heater surface was covered by the spray with little

overspray. The flow rate through the nozzle was set at 11 ml/min, 24 ml/min, and 37 ml/min. The corresponding volumetric fluxes are 0.0037 m^3/m^2-s, 0.0082 m^3/m^2-s, and 0.0126 m^3/m^2-s. A summary of the test conditions to be discussed in presented on Table 4.1. For Case 5, air was pumped into the flow loop to increase the pressure above atmospheric.

Table 4.1: Summary of test conditions for spray cooling tests.

Case No.	$T_{reservoir}$ (°C)	T_{spray} (°C)	$P_{reservoir}$ (atm)	T_{sat} (°C)	TS (°C)	GS (°C)	Comments
1	23.5	25	0.33	27.1	-1.5	3.6	Nominally degassed, saturated liquid.
2	22.5	1.4	0.33	27.1	21.1	4.6	Nominally degassed, thermal subcooling.
3	23.2	25	0.67	45.5	-1.8	22.3	Gassy subcooling comparable to thermal subcooling of Case 2.
4	24	25	1.0	56.7	-1	32.7	Test rig at nominally 1 atm, gassy subcooling.
5	24	25	1.22	63.6	-1	39.6	Test rig above 1 atm, gassy subcooling.

4.3.1 Effect of thermal subcooling on degassed fluid

Spray cooling curves showing the effect of thermal subcooling on nominally degassed fluid are shown on Figure 4.2. Thermal subcooling is shown to increase the heat transfer for a given flow rate due to addition of sensible heating required to bring the fluid up to the saturation pressure, and is consistent with the results of previous researchers. The temperature at which CHF occurs is not dependent on thermal subcooling.

4.3.2   Effect of dissolved gas

The effect of varying amounts of dissolved gas on spray cooling at the maximum flow rate tested are shown on Figure 4.3. It is observed that as the dissolved gas content increases, the spray cooling curves shift to the right and the CHF increases, consistent with the trends observed by Lin and Ponnappan (2002). The shift to higher temperatures is a direct consequence of the increase in T_{sat} when dissolved gas is present, which effectively subcools the liquid. The data for the highest gas content cases (Cases 4 and 5) merge for T_{wall}=50 °C and T_{wall}=55 °C in Figure 4.3 as expected since the wall temperature is below the saturation temperature and heat is transferred by only single phase fluid, although there may be a small contribution from evaporation. The
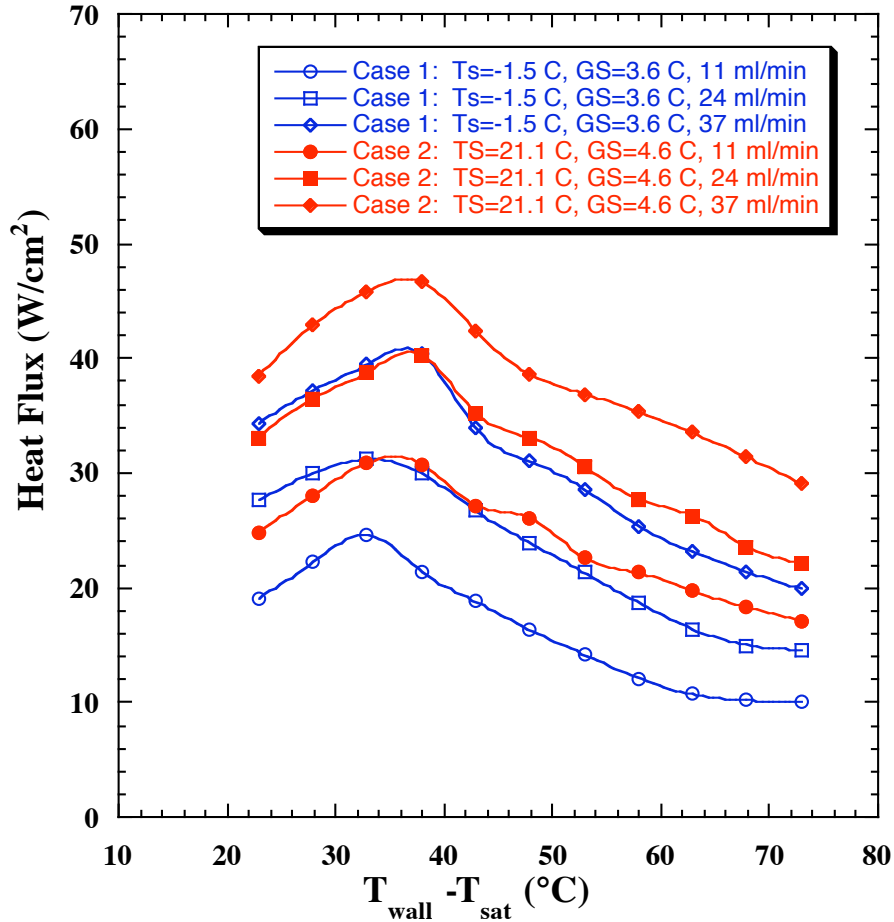
Figure 4.2: Thermal subcooling effects on spray cooling heat transfer.

liquid for Case 3 at T_{wall}=50 °C is slightly superheated, and this is reflected in the slightly increased heat transfer above the data for Cases 4 and 5. The data for Cases 1 and 2 (degassed liquid) are significantly higher, indicating that evaporation plays a major role in spray heat transfer.

The same heat transfer data plotted vs. the wall superheat instead of wall temperature to remove the effect of changes in T_{sat} with gas content is shown on Figure 4.4. Comparison of Case 2 (TotS=25.7 °C, predominantly thermally subcooled) and Case 3 (TotS=20.5 °C, predominantly gas subcooled) on this figure reveals the role of gas at roughly similar TotS levels. Even though TotS for Case 2 is larger than TotS for Case 3, higher heat transfer is observed for Case 3 at a given superheat, indicating the gas has an effect in addition to the subcooling effect. The presence of gas may cause additional single phase convection over the heater areas not covered by drops, or can contribute additional evaporation of the liquid. The gas
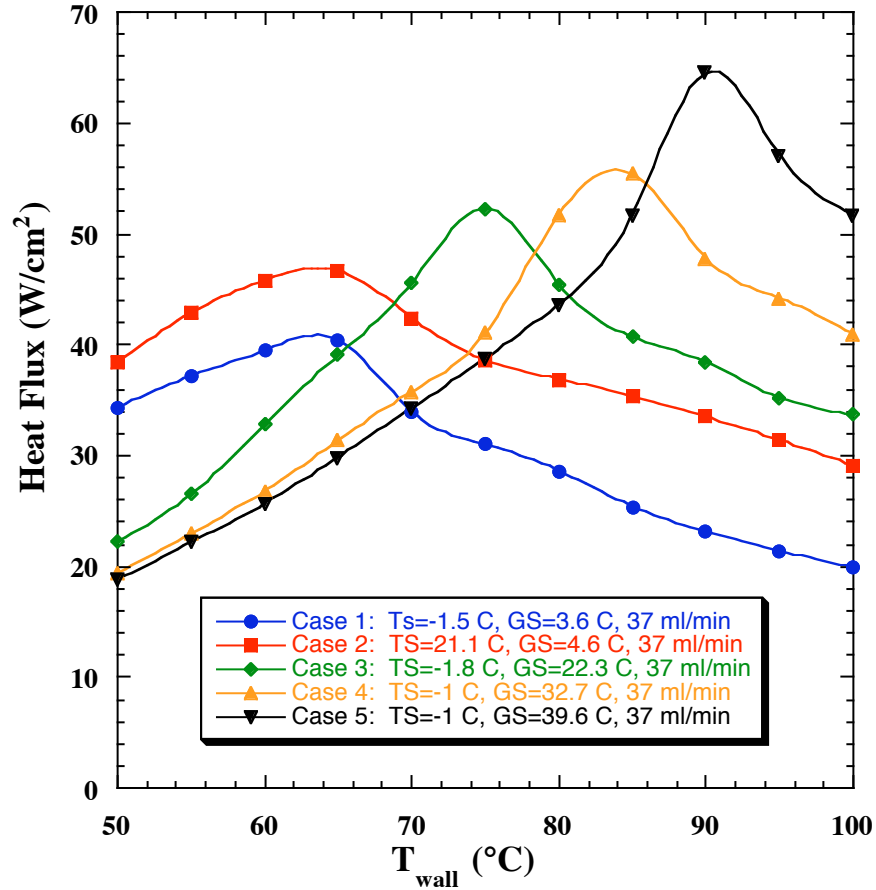
Figure 4.3: Effect of dissolved gas for flow rate of 37 ml/min.

may cause bubbles to nucleate within the drops, spreading the drops over a larger heater area thereby increasing the liquid-solid contact area or by increasing the liquid-vapor contact area as observed for the single drops, increasing the heat transfer. The gas could also increase theconduction through the drop by reducing T_{sat}. Evaluation of each of these mechanisms is currently under investigation.

This data suggests that it may be advantageous under certain circumstances to operate with dissolved gas if enough condenser area is available. For example, it may be desirable to operate using a gassy fluid with a lower boiling point so higher CHF levels can be obtained while still keeping the wall temperature within acceptable limits. However, the condenser must be large enough to condense the vapor generated even in the presence of gas.
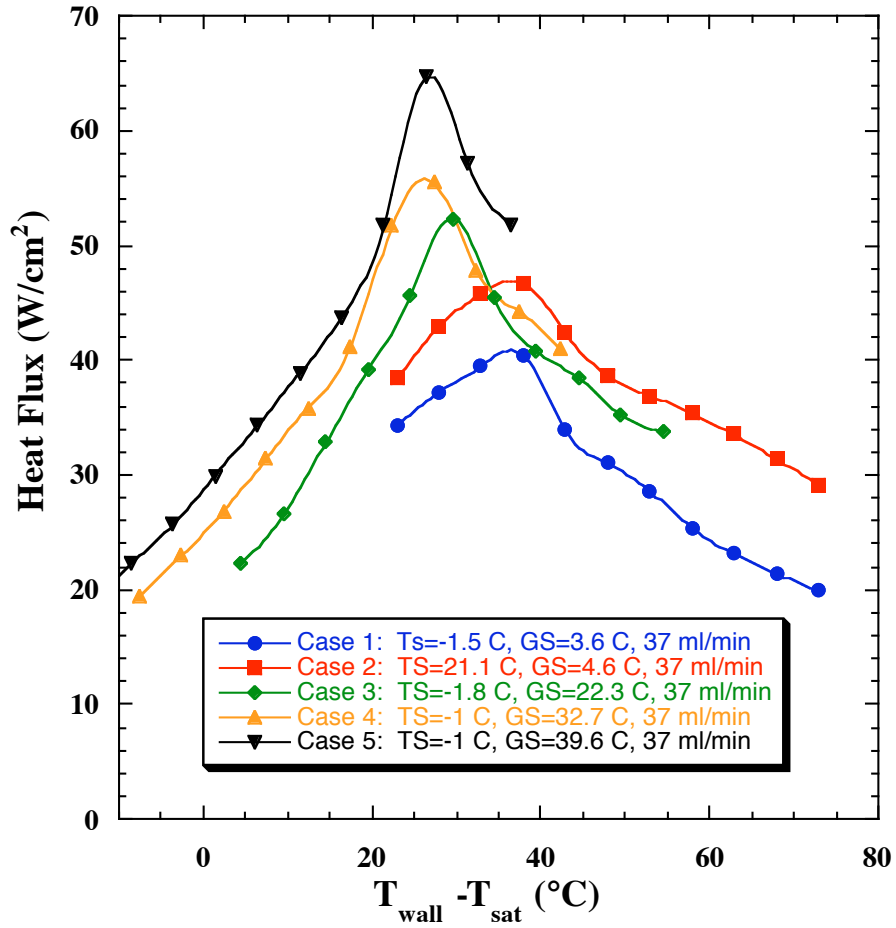
Figure 4.4: Effect of dissolved gas for flow rate of 37 ml/min in terms of wall superheat.

5. CONCLUSIONS

An experimental technique using an array of microscale heaters and high-speed imaging has been used to examine the time and space resolved heat flux and dynamics of the droplet vaporization process on an isothermal wall. The experiments were performed with PF-5060 in ambient air, with a fixed impact diameter (0.82 mm) and velocity (0.3 m/s), but at three different superheats ($T_w - T_{sat}$ = 9 °C, 19 °C and 29 °C). Droplets with and without gas were studied. When the heat flux data is expressed in terms of an effective heat transfer coefficient, h, the results show that the droplet vaporization process can be divided into two distinct parts: the first part corresponds to a transient fluctuation of h, while the second is characterized by a constant value of h. The initial transient is likely to be caused by a combination of the initial heat conduction into the liquid, the oscillatory motion of the droplet, and the establishment of a vapor concentration boundary layer at the liquid-vapor interface. The present work was not able to discern the exact contribution from each of these components. The second part of the vaporization process, corresponding to a constant h, is consistent with a perspective in which the heat transfer rate is limited by the external diffusion/convection resistance of the vapor away from the droplet. Comparisons made to the constant contact angle (moving contact line) models yielded very good agreement for the rate of change of the splat diameter during this regime, until the final 10 % of the evaporation time. Thus for droplets with these specific impact conditions, the existing models for low superheat vaporization are adequate to predict approximately 65% of the droplet's lifetime. Continued work needs to be focused on the prediction of the transient h regime, particularly if advances are to be made in spray cooling applications where the droplets are typically much smaller. Under these conditions, the droplet evaporation process may be short enough such that it is wholly dominated by the transient process.

Data was also obtained with drops containing gas. The bubbles that formed within the drops very early after impact either burst soon after impact or coalesced to form large primary bubble within the drop. The primary bubble burst at various times during the evaporation process. Formation of bubbles within the drop was found to increase the wall heat transfer and decrease the drop lifetime. The wall heat transfer due to an evaporating drop was found to be

primarily dependent to the liquid-vapor contact area, indicating that the vapor removal process is the limiting thermal resistance.

Recent spray cooling measurements indicate that dissolved gas shifts the heat transfer curve to higher wall temperatures due to the increase in the saturation temperature. Higher CHF values were also observed, indicating that it may be desirable to operate with gassy fluid under certain circumstances. Additional work is required to clarify the mechanisms by which the gas alters the heat transfer.

6. REFERENCES

3M Corporation, 1995, *3M Specialty Fluids Newsletter,* Vol. 1, No. 1, April, 1995

Bae, S., Kim, M. H., and Kim, J., 1999, Improved Technique to Measure Time and Space−Resolved Heat Transfer under Single Bubbles during Saturated Pool Boiling of FC-72, *Exp. Heat Transfer*, **12**, 265-278.

Bolle, L., and Moureau, J. C., 1982, Spray Cooling of Hot Surfaces, *Multiphase Science and Technology*, Vol. 1, Hemisphere, Washington DC, 1-97.

Bonacina, C., Del Giudice, S., and Comini, G., 1979, Dropwise Evaporation, *J. Heat Transfer*, **101**, 441-446.

Chen, J. C., Sundaram, R. K., and Ozkaynak, F. T., 1977*, A Phenomenological Correlation for Post-CHF Heat Transfer*, Technical Report for USNRC, Contract No. AT(49-24)-0180, Lehigh University, Bethlehem, PA.

Choi, K. J., and Yao, S. C., 1987, Mechanism of Film Boiling Heat Transfer of Normally Impacting Spray, *Int. J. Heat Mass Transfer*, **30**, 311-318.

Cui, Q., Chandra, S., McCahan, S. "Enhanced boiling of water droplets containing dissolved gases or solids", Paper No. NHTC 2000-12249, National Heat Transfer Conference, Pittsburgh, Pennsylvania, August 20-22, (2000)

diMarzo, M., and Evans, D. D., 1989, Evaporation of a Water Droplet Deposited on a Hot High Thermal Conductivity Surface, *J. Heat Transfer*, **111**, 210-221.

di Marzo, M., Tartarini, P., Liao, Y., Evans, D., and Baum, H., 1993, Evaporative Cooling Due to a Gently Deposited Droplet, *Int. J. Heat Mass Transfer*, **36**, 4133-4139.

Kline, S. J., and McClintock, F. A., 1953, Describing Uncertainties in Single-Sample Experiments, *Mech. Engg*, **75**, 3-8.

Lin, L, and Ponnappan, R. (2002), "Heat transfer characteristics of an evaporative spray cooling in a closed loop", Proceedings of the 2002 SAE Power Systems Conference, Coral Springs, FL, SAE Paper No. 2002-01-3198.

Liu, L., and Yao, S. C., 1982, Heat Transfer Analysis of Droplet Flow Impinging on a Hot Surface, *Proc. 7th Int. Heat Transfer Conf.*, Munich, Germany, Vol. 4, 161-166.

McGinnis, F. K., and Holman, J. P., 1969, Individual Droplet Heat Transfer Rates for Splattering on Hot Surfaces, *Int. J. of Heat Mass Transfer*, **12**, 95-108.

Milke, J.A., Tinker, S.C., and diMarzo, M., "Effect of dissolved gases on spray evaporative cooling with water", Fire Technology, 2nd Quarter, Vol. 33, No. 2, May/June, 1997.

Qiao, Y. M. and Chandra, S., 1997, Experiment on Adding a Surfactant to Water Drops Boiling on a Hot Surface, *Proc. Royal Soc. London A*, **453**, 673-689.

Råde, L. and Westergren, B., 1995, *Mathematics Handbook for Science and Engineering*, Birkhäuser, Sweden.

Rainey, K.N., You, S.M, and Lee, S. (2003), "Effect of Pressure, Subcooling, and Dissolved Gas on Pool Boiling Heat Transfer From Microporous Surfaces in FC-72", Journal of Heat Transfer, Vol 125, pp. 75-83.

Rule, T. D., and Kim, J., 1999, Heat Transfer Behavior on Small Horizontal Heaters During Pool Boiling of FC-72, *J. Heat Transfer*, **121**, 386-393.

Rule, T. D., Kim, J., and Kalkur, T. S., 1998, Design, Construction, and Qualification of a Microscale Heater Array for Use in Boiling Heat Transfer, NASA/CR-1998-207407.

Rule, T. D., Kim, J., Quine, R. W., Kalkur, T. S., and Chung, J. N., 1999, Measurements of Spatially and Temporally Resolved Heat Transfer Coefficients in Subcooled Pool Boiling, *Convective Flow and Pool Boiling*, Taylor and Francis.

Sadhal, S. S., Ayyaswamy, P. S., and Chung, J. N., 1997, *Transport Phenomena with drops and Bubbles*, Springer-Verlag, New York.

Sadhal, S. S. and Plesset, M. S., 1979, Effect of Solid Properties and Contact Angle in Dropwise Condensation and Evaporation, *J. Heat Transfer*, **101**, 48-54.

Tilton, D.E., Tilton, C.L, Pais, M.R., and Morgan, M.J. (1992), "High-Flux Spray Cooling in a Simulated Multichip Module", HTD-Vol. 206-2, Proceedings of the 1992 ASME Heat Transfer Conference.

Toda, S., 1972, A Study of Mist Cooling (1st Report: Investigation of Mist Cooling), *Heat Transfer-Japanese Research*, **1**, 39-50.

Toda, S., 1974, A Study of Mist Cooling (1st Report: Theory of Mist Cooling and Its Fundamental Experiments), *Heat Transfer-Japanese Research*, **3**, 1-44.

Wachters, L. H. J., Bonne, H, and van Nouhuis, H. J., 1966a, The Heat Transfer from a Hot Horizontal Plate to Sessile Water Drops in the Spheroidal State, *Chem. Eng. Sci.*, **21**, 923-936.

Wachters, L. H. J., and Westerling, N. A. J., 1966b, The Heat Transfer from a Hot Wall to Impinging Water Drops in the Spheroidal State, *Chem. Eng. Sci.*, **21**, 1047-1056.